A&A, 707, A321 (2026)
https://doi.org/10.1051/0004-6361/202558023
© The Authors 2026

Astronomy & Astrophysics

Near-degeneracy effects in quadrupolar mixed modes

From an asymptotic description to data fitting

B. Liagre[1,2,3,⋆], A. Desai[1], L. Einramhof[1], and L. Bugnet[1]

[1] Institute of Science and Technology Austria (ISTA), Am Campus 1, 3400 Klosterneuburg, Austria
[2] Université Paris Cité, Université Paris-Saclay, CEA, CNRS, AIM, 91191 Gif-sur-Yvette, France
[3] Instituto de Astrofísica de Canarias (IAC), E-38205 La Laguna, Tenerife, Spain

Received 7 November 2025 / Accepted 14 January 2026

ABSTRACT

Dipolar ($\ell = 1$) mixed modes have revealed a surprisingly weak differential rotation between the core and the envelope of evolved solar-like stars. Quadrupolar ($\ell = 2$) mixed modes also contain information regarding internal dynamics but are very rarely characterised due to their low amplitude and the challenging identification of adjacent or overlapping rotationally split multiplets affected by near-degeneracy effects. We aim to extend the broadly used asymptotic seismic diagnostics beyond $\ell = 1$ mixed modes by developing an analogue asymptotic description of $\ell = 2$ mixed modes while explicitly accounting for near-degeneracy effects that distort their rotational multiplets. We have derived a new asymptotic formulation of near-degenerate mixed $\ell = 2$ modes that describes off-diagonal terms representing the interaction between modes of adjacent radial orders. This formalism, expressed directly in the mixed-mode basis, provides analytical expressions for the near-degeneracy effects. We implemented the formalism within a global Bayesian mode-fitting framework for a direct fit of all $\ell = 0, 1, 2$ modes in the power spectrum density. We were able to asymptotically model the asymmetric rotational splitting present in various radial orders of $\ell = 2$ modes observed in young red giant stars without the need for any numerical stellar modelling. We applied our formalism to the *Kepler* target KIC 7341231, and it yielded core and envelope rotation rates consistent with previous numerical modelling while providing improved constraints from the global and model-independent approach. We also characterised the new target, KIC 8179973, measuring its rotation rate and mixed-mode parameters for the first time. As our framework relies on a direct global fit, it allows for much better precision on the asteroseismic parameters and rotation rate estimates than standard methods, yielding better constraints for rotation inversions. We have placed the first observational constraints on the asymptotic $\ell = 2$ mixed-mode parameters ($\Delta\Pi_2$, q_2, and $\varepsilon_{g,2}$), thus paving the way towards the use of asymptotic seismology beyond $\ell = 1$ mixed modes.

Key words. asteroseismology – methods: analytical – methods: data analysis – stars: oscillations – stars: rotation – stars: solar-type

1. Introduction

Understanding the internal dynamics of evolved solar-like stars remains one of the major challenges in asteroseismology. Internal dynamical processes can be probed using oscillations that consist of acoustic pressure modes (p modes) and buoyancy-driven gravity modes (g modes). In evolved solar-like stars, p and g modes can couple across their respective cavities, giving rise to mixed modes (e.g. Unno et al. 1989; Takata 2016a), first detected by Beck et al. (2011). Mixed-mode analyses have revealed the core and the envelope rotation rates of sub-giant and red giant stars (e.g. Beck et al. 2011; Deheuvels et al. 2012; Mosser et al. 2012a; Deheuvels et al. 2014; Di Mauro et al. 2016; Gehan et al. 2018; Li et al. 2024). However, measured rotational gradients are substantially weaker than those predicted by hydrodynamical theoretical models of angular momentum evolution (e.g. Eggenberger et al. 2012; Marques et al. 2013; Ceillier et al. 2013; Eggenberger et al. 2017, 2019). This discrepancy indicates the presence of missing angular momentum transport mechanisms in our representation of angular momentum transport in stars. Several processes have been proposed to enhance transport, including meridional circulation (Zahn 1992; Maeder & Zahn 1998; Mathis & Zahn 2004; Decressin et al. 2009), hydrodynamical instabilities (Zahn 1992), mixed modes (Belkacem et al. 2015; Bordadágua et al. 2025), internal gravity waves (Schatzman 1993; Fuller et al. 2014; Pinçon et al. 2017; Rogers & Ratnasingam 2025), and magnetic processes such as transport by Alfvén waves and magnetic tension (e.g. Mestel & Weiss 1987; Zahn et al. 2007; Takahashi & Langer 2021; Gouhier et al. 2022), magneto-rotational instabilities (Meduri et al. 2024), magnetic webs (Skoutnev & Beloborodov 2025a), or transport by the Tayler-Spruit dynamo (e.g. Tayler 1973; Spruit 2002; Fuller et al. 2019; Moyano et al. 2023; Skoutnev & Beloborodov 2025b). To date, no observational constraints have unequivocally identified any overarching dominant physical mechanism responsible for angular momentum transport along stellar evolution.

To better constrain the efficiency of such newly proposed angular momentum transport mechanisms, more refined seismic diagnostics are required. So far, most efforts to constrain stellar internal rotation rates have focused on dipolar mixed modes, i.e. modes with degree $\ell = 1$. Extending the analysis beyond dipole ($\ell = 1$) modes to include quadrupole mixed modes ($\ell = 2$) offers the prospect of significantly strengthening and adding constraints on internal dynamics. This extension not only increases the number of available observational probes but also provides sensitivity to different dynamical kernels, as modes of different degrees sample distinct regions of the stellar interior, particularly

⋆ Corresponding author: bastien.liagre@cea.fr

Open Access article, published by EDP Sciences, under the terms of the Creative Commons Attribution License (https://creativecommons.org/licenses/by/4.0), which permits unrestricted use, distribution, and reproduction in any medium, provided the original work is properly cited.
This article is published in open access under the Subscribe to Open model. Subscribe to A&A to support open access publication.

within the convective zone (Hekker & Christensen-Dalsgaard 2017). The probing power of $\ell = 2$ mixed modes and our ability to use them are limited by two major factors: (i) The p- and g-mode cavities sit further away from each other than those of $\ell = 1$ modes, leading to an expected much weaker coupling strength that reduces the height of the $\ell = 2$ mixed modes in the power spectral density (hereafter PSD, Dupret et al. 2009; Grosjean et al. 2014; Mosser et al. 2018). (ii) The presence of near-degeneracy effects between adjacent multiplets distort the splitting structure (Lynden-Bell & Ostriker 1967; Dziembowski & Goode 1992; Deheuvels et al. 2012, 2014, 2017; Mosser et al. 2018; Ong et al. 2022; Li et al. 2024; Ahlborn et al. 2025) and prevent straightforward identification and interpretation of the $\ell = 2$ mixed-mode frequency pattern.

While the above-mentioned point (i) is a detectability limit, point (ii) reduces our ability to identify modes. Standard first-order perturbation theory predicts symmetric splittings in slowly-rotating stars (e.g. Aerts et al. 2010; Goupil et al. 2013; Deheuvels et al. 2014; Gehan et al. 2018). However, if two unperturbed modes are close in frequency, their eigenfunctions are no longer independent. The resulting near-degeneracy introduces off-diagonal interaction terms in the oscillation equations, producing an observable asymmetry in the mixed-mode frequency pattern (Lynden-Bell & Ostriker 1967; Dziembowski & Goode 1992; Deheuvels et al. 2017; Mosser et al. 2018; Ong et al. 2022; Li et al. 2024; Ahlborn et al. 2025). Despite several studies investigating near-degeneracy effects on oscillation frequencies (e.g. Deheuvels et al. 2017; Mosser et al. 2018; Ong et al. 2022; Li et al. 2024; Ahlborn et al. 2025) and efforts to include $\ell = 2$ modes in seismic analysis (Deheuvels et al. 2012, 2014, 2017; Benomar et al. 2013), no asymptotic framework has been developed yet to explicitly compute the near-degeneracy interaction terms in the mixed-mode basis. For instance, Li et al. (2024) performed an implicit treatment of these effects, while Ong et al. (2022) carried out the calculation in the π–γ decoupled mode basis. In this work, we present a new asymptotic formalism for mixed quadrupole modes that explicitly incorporates near-degeneracy effects through non-diagonal near-degeneracy terms in the mixed-mode basis. This approach enables us to compute the near-degeneracy terms directly in the asymptotic limit and solve the associated quadratic eigenvalue problem. It also offers two main advantages: (i) It preserves the mixed-mode basis, which simplifies the implementation for direct use in data analysis, similar to the method extensively used to analyse $\ell = 1$ mixed modes. (ii) It provides explicit asymptotic estimates of the off-diagonal near-degeneracy terms, allowing for closed-form near-degeneracy corrections derived from quantum perturbation theory.

This article is structured as follows: In Section 2 we lay the theoretical basis for this work and show the development leading to the asymptotic expression of the off-diagonal near-degeneracy terms. In Section 3, we introduce the global Bayesian framework and the priors we used for simultaneously fitting of our radial and $\ell = 1, 2$ mixed modes. Finally, in Section 4 we describe how we applied our new formalism and analysis pipeline to two early red giant stars observed by the NASA *Kepler* mission (Borucki et al. 2010). We started with KIC 7341231, which has already been characterised with numerical methods by Deheuvels et al. (2017), to demonstrate the robustness of our prescription. We then performed the global fit of mixed modes in the new candidate, KIC 8179973, which shows strong near-degeneracy effects in the quadrupolar modes. We report our results before concluding in Section 5.

2. New developments on near degeneracy effects

2.1. Theoretical context

We begin by outlining the theoretical background and notation underlying our new asymptotic formulation. This framework was developed within the standard theory of adiabatic stellar oscillations.

2.1.1. The general rotating eigenvalue problem

As shown in, for example, Aerts et al. (2010), in the case of a non-rotating spherical star, the stellar adiabatic oscillation problem can be cast as an eigenvalue equation:

$$\frac{\partial^2 \boldsymbol{\delta r}}{\partial t^2} = \hat{\mathcal{L}}\,\boldsymbol{\delta r}, \tag{1}$$

where $\hat{\mathcal{L}}$ denotes the linear operator that encapsulates the perturbations of the equilibrium due to volumetric forces and acts on the displacement field $\boldsymbol{\delta r}$ associated with stellar oscillations:

$$\hat{\mathcal{L}}\,\boldsymbol{\delta r} = \frac{\nabla p'}{\rho} + \nabla\Phi' - \frac{\rho'}{\rho^2}\nabla p. \tag{2}$$

Here, ρ and p are the equilibrium pressure and density of the star, while p', ρ', and Φ' are the Eulerian perturbations in pressure, density, and gravitational potential.

The solutions of this eigenvalue problem are given by a set of eigenvalues, $\omega_{0,n,\ell,m}$, and eigenfunctions, $\boldsymbol{\delta r}_{0,n,\ell,m}$, that can be decomposed on the spherical harmonics basis as

$$\boldsymbol{\delta r}_{0,n,\ell,m} = \left[\xi_{0,r,\ell,n,m}(r) Y_\ell^m(\theta,\phi)\boldsymbol{e}_r + \xi_{0,h,\ell,n,m}(r)\left(\frac{\partial Y_\ell^m}{\partial\theta}\boldsymbol{e}_\theta + \frac{1}{\sin(\theta)}\frac{\partial Y_\ell^m}{\partial\varphi}\boldsymbol{e}_\varphi\right)\right]\exp(-i\omega_{0,n,\ell,m}t). \tag{3}$$

In this basis, n is the number of nodes of the eigenfunction along the radius, ℓ is the angular degree, and m is the azimuthal order of the mode.

In the absence of any perturbation that breaks the spherical symmetry of the initial problem, the modes with the same radial order, n, and angular degree, ℓ, but different azimuthal order, m, are degenerate in frequency such that $\omega_{0,n,\ell} = \omega_{0,n,\ell,m}\ \forall m$. In the rest of the article, we refer to these eigenfunctions as unperturbed eigenfunctions. We index them by their n only, as our physical framework does not allow for coupling between modes of different degrees (ℓ). Hence, the set of unperturbed eigenfunctions is the set of all $\boldsymbol{\delta r}_{0,i} = \boldsymbol{\delta r}_{0,i,\ell,m}$, with eigenvalues $\omega_{0,i} = \omega_{0,i,\ell,m}$, where i plays the role of n such that

$$\boldsymbol{\delta r}_{0,i} = \left[\xi_{0,r,i}(r) Y_\ell^m(\theta,\phi)\boldsymbol{e}_r + \xi_{0,h,i}(r)\left(\frac{\partial Y_\ell^m}{\partial\theta}\boldsymbol{e}_\theta + \frac{1}{\sin(\theta)}\frac{\partial Y_\ell^m}{\partial\varphi}\boldsymbol{e}_\varphi\right)\right]\exp(-i\omega_{0,i}t). \tag{4}$$

In this equation, the r index refers to the part of the eigenfunction that oscillates vertically along the radius, while the h index refers to the horizontally oscillating part of the eigenfunction.

When including stellar rotation into the motion equation, the spherical-symmetry-induced degeneracy is lifted, and the solutions to the eigenvalue problem depend on m. At the leading order in Ω, i.e. the angular rotation rate of the star, the eigenvalue problem becomes (e.g. Aerts et al. 2010; Deheuvels et al. 2017; Ahlborn et al. 2025)

$$-\omega^2\,\boldsymbol{\delta r} + 2\omega\,(m\Omega - i\,\boldsymbol{\Omega}\times)\,\boldsymbol{\delta r} = \left(-\omega^2 + \omega\hat{\mathcal{L}}_{\mathrm{rot},m}\right)\boldsymbol{\delta r} = \hat{\mathcal{L}}\,\boldsymbol{\delta r}, \tag{5}$$

where we assumed $\mathbf{\Omega} = \Omega(r,\theta)\,(\cos(\theta)\boldsymbol{e}_r - \sin(\theta)\boldsymbol{e}_\theta)$, and where $\boldsymbol{\delta r}$ is the perturbed eigenfunction.

We then decomposed $\boldsymbol{\delta r}$ on the basis of the unperturbed eigenmodes such as

$$\frac{\boldsymbol{\delta r}}{\sqrt{I}} = \sum_i \frac{a_i}{\sqrt{I_{0,i}}}\,\boldsymbol{\delta r}_{0,i}, \tag{6}$$

with

$$I = \langle \boldsymbol{\delta r}, \boldsymbol{\delta r}\rangle, \tag{7}$$

where $\langle\cdot,\cdot\rangle$ is the inner product defined as (for two vectors $\boldsymbol{a}$ and $\boldsymbol{b}$ and ρ the local density of the star)

$$\langle \boldsymbol{a}, \boldsymbol{b}\rangle = \int_{\text{star}} \rho \boldsymbol{a}^* \boldsymbol{b}\,\mathrm{d}^3 r. \tag{8}$$

Thus Eq. (5) can be written in a matrix form:

$$\omega^2 \mathbb{I}\boldsymbol{a} - \omega \mathbf{R}\boldsymbol{a} - \mathbf{L}\boldsymbol{a} = 0, \tag{9}$$

where $\mathbb{I}$ is the identity matrix, $\mathbf{L} = \mathrm{diag}(\omega_{0,i}^2)$, $\boldsymbol{a}$ is the vector of the a_i (i.e. the coefficients of the decomposition of $\boldsymbol{\delta r}$ in the unperturbed base following Eq. (6)), and

$$R_{i,j} = \frac{\langle \boldsymbol{\delta r}_{0,i}, \hat{\mathcal{L}}_{\text{rot},m}\boldsymbol{\delta r}_{0,j}\rangle}{\sqrt{I_{0,i} I_{0,j}}}. \tag{10}$$

Assuming a rotational profile that only depends on the radius of the star $\Omega = \Omega(r)$, the matrix elements of R can be written as (e.g. Deheuvels et al. 2017)

$$\langle \boldsymbol{\delta r}_{0,i}, \hat{\mathcal{L}}_{\text{rot},m}\boldsymbol{\delta r}_{0,j}\rangle = 2m \int_{\text{star}} K_{i,j}(r)\Omega(r)\mathrm{d}r, \tag{11}$$

with

$$K_{i,j}(r) = \rho r^2 \times \left(\xi^*_{0,r,i}\xi_{0,r,j} + (L^2-1)\xi^*_{0,h,i}\xi_{0,h,j} - \xi^*_{0,h,i}\xi_{0,r,j} - \xi^*_{0,r,i}\xi_{0,h,j}\right), \tag{12}$$

where we have introduced the notation $L = \sqrt{\ell(\ell+1)}$ and where $\boldsymbol{\delta r}_{0,i}$ and $\boldsymbol{\delta r}_{0,j}$ are the eigenfunctions of two mixed modes unperturbed by rotation.

2.1.2. The two-zone rotating model

In the rest of the developments, we use the general expression for the matrix elements $R_{i,j}$ and discuss the simplifications that arise under the assumption of a two-zone rotation model. As is customary in the literature (e.g. Mosser et al. 2012a; Gehan et al. 2018), we now consider a simplified model of rotation with two zones – the core (i.e. the g-mode cavity) and the envelope (i.e. the p-mode cavity) – rotating at fixed rotational rates Ω_{core} and Ω_{env}, respectively.

2.2. First order symmetric rotational effects: Diagonal terms

At the first perturbative order (i.e. neglecting the coupling elements between eigenmodes of different n), an eigenfrequency will symmetrically lift its degeneracy and create what we refer to as a rotational splitting of width (e.g. Aerts et al. 2010; Unno et al. 1989):

$$\omega_i - \omega_{0,i} = \delta\omega_i = \frac{1}{2I}\left\langle \boldsymbol{\delta r}_{0,i}, \hat{\mathcal{L}}_{\text{rot},m}\boldsymbol{\delta r}_{0,i}\right\rangle. \tag{13}$$

The modes of the same ℓ and different m are no longer at the same frequency but are at first order distributed symmetrically around the peak of $m = 0$.

The coupling element,

$$\frac{1}{I}\left\langle \boldsymbol{\delta r}_{0,i}, \hat{\mathcal{L}}_{\text{rot},m}\boldsymbol{\delta r}_{0,i}\right\rangle, \tag{14}$$

may be asymptotically expressed using the seismic ζ function. For a given unperturbed mixed mode, the asymptotic expression of the ζ-function provides the ratio between the mode inertia in the g-mode cavity and the total mode inertia (Goupil et al. 2013, see also Section 3.1.3 for the asymptotic expression of this quantity):

$$\zeta(\omega) = \frac{I_{\text{g}}}{I}. \tag{15}$$

Based on this relation, the asymptotic expressions for the diagonal elements of the coupling matrix within the two-zone model were shown to be given by Goupil et al. (2013), Deheuvels et al. (2014)

$$\frac{\left\langle \boldsymbol{\delta r}_{0,i}, \hat{\mathcal{L}}_{\text{rot},m}\boldsymbol{\delta r}_{0,i}\right\rangle}{I_{0,i}} = 2m \times \Big(\Omega_{\text{core}}\zeta(\omega_{0,i})\Big(1 - \frac{1}{L^2}\Big) + \Omega_{\text{env}}(1-\zeta(\omega_{0,i}))\Big). \tag{16}$$

We use this description, excluding near-degeneracy effects (i.e. off-diagonal near-degeneracy terms), to fit the $\ell = 1$ modes in Sect. 4 because the targets we chose have a large frequency separation, $\Delta\nu > 20$, where we expect little to no influence of near-degeneracy effects (Ahlborn et al. 2025). In the case of more evolved stars in the regime of low asymmetry splittings (typically for $11 < \Delta\nu < 13$, depending on the core rotation rate according to Ahlborn et al. 2025), our framework provides an explicit second-order perturbative correction to the rotational splitting (based on Eq. (27), see Appendix A for more details).

This approach eliminates the need to solve the implicit equation used by Li et al. (2024) to reproduce the rotational asymmetries in $\ell = 1$ mode splittings.

2.3. Near-degeneracy effects: Non-diagonal terms

The symmetry in the splitting of the modes can be broken when the non-diagonal elements (i.e. $i \neq j$) of the matrix, R, become non-negligible compared to the diagonal. This is expected to happen when two modes have a frequency separation comparable to the rotation rate of the star, i.e. when $|\omega_i - \omega_j| \sim \Omega$ (Dziembowski & Goode 1992; Deheuvels et al. 2017; Ahlborn et al. 2025). This is illustrated in Fig. 1, which uses the asymptotic framework of this paper to highlight how near-degenerate interactions modify the usual pattern of rotationally split multiplets and generate asymmetries in the frequency pattern.

The off-diagonal terms, which are those responsible for the near-degeneracy asymmetry effects, can be written as (Deheuvels et al. 2017)

$$\frac{\left\langle \boldsymbol{\delta r}_{0,i}, \hat{\mathcal{L}}_{\text{rot},m}\boldsymbol{\delta r}_{0,j}\right\rangle}{\sqrt{I_{0,i}I_{0,j}}} = 2m\left(\gamma_{c,ij}\Omega_{\text{core}} + \gamma_{e,ij}\Omega_{\text{env}}\right), \tag{17}$$

with

$$\gamma_{c,ij} = \frac{1}{\sqrt{I_{0,i}I_{0,j}}}\int_{\text{g}} K_{i,j}(r)\mathrm{d}r \tag{18}$$

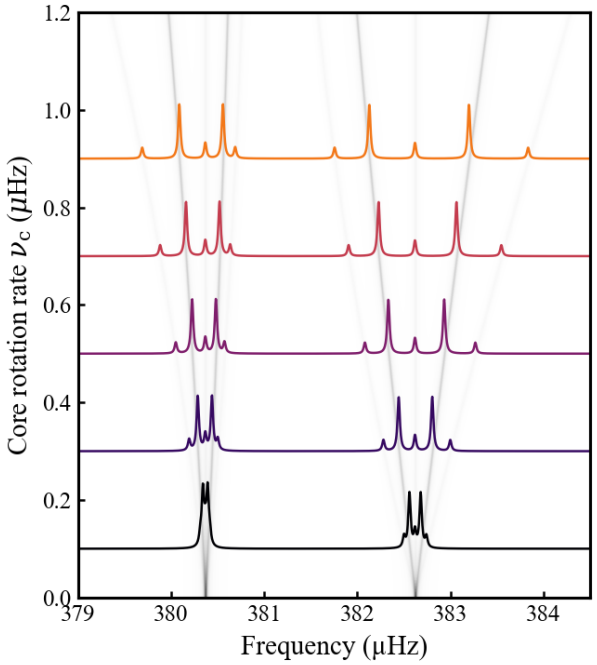

Fig. 1. Illustration of the effect of near degeneracy on two coupled $\ell = 2$ multiplets as the core rotation rate $\nu_c = \Omega_{\rm core}/2\pi$ increases for a fixed inclination angle of $i = 42°$. Each horizontally modelled PSD shows the combined visibility profile of the ten components (two sets of $m = -2, -1, 0, +1, +2$ modes) at a given ν_c. The greyscale background indicates how the multiplet structure evolves continuously with rotation.

and

$$\gamma_{e,ij} = \frac{1}{\sqrt{I_{0,i}I_{0,j}}} \int_{\rm p} K_{i,j}(r)\mathrm{d}r. \tag{19}$$

Because the mixed-mode basis is orthogonal and the oscillation verify $\xi_r \ll \xi_h$ (resp. $\xi_r \gg \xi_h$) in the g-mode cavity (resp. p-mode cavity) (e.g. Aerts et al. 2010; Bugnet et al. 2021; Mathis et al. 2021), Deheuvels et al. (2017) showed that

$$\gamma_{c,ij} = \frac{1}{\sqrt{I_{0,i}I_{0,j}}} \int_{\rm g} \rho r^2 (L^2-1) \xi^*_{0,h,i}\xi_{0,h,j}\mathrm{d}r, \tag{20}$$

and

$$\gamma_{e,ij} = \frac{L^2}{1-L^2}\gamma_{c,ij}. \tag{21}$$

Hence, in order to describe the off-diagonal terms of the eigenvalue problem, it is sufficient to evaluate $\gamma_{c,ij}$.

2.3.1. New asymptotic formula for the near degeneracy effects

To find an asymptotic formula for $\gamma_{c,ij}$ that could be applied to fit observations, we used the asymptotic Jeffreys-Wentzel–Kramers–Brillouin (e.g. Jeffreys 1925; Wentzel 1926) form of the horizontal eigenfunctions in the g-mode cavity as given in, for example, Mathis et al. (2021):

$$\xi_h = -\frac{A}{\sqrt{L}\omega}\rho^{-1/2}r^{-3/2}\left(\frac{N^2}{\omega^2}\right)^{1/4} \sin\left(L\int_0^r \frac{N}{\omega}\frac{\mathrm{d}r'}{r'} - \frac{\pi}{4}\right), \tag{22}$$

where A is the amplitude of the mode and N is the Brunt–Väisälä frequency. This yields

$$\gamma_{c,ij} = \frac{1}{\sqrt{I_{0,i}I_{0,j}}} \int_{\rm g} \frac{A_{0,i,g}A_{0,j,g}(L^2-1)}{L\sqrt{\omega^3_{0,i}\omega^3_{0,j}}}\frac{N}{r} \times \sin\left(L\int_0^r \frac{N}{r'}\mathrm{d}r'\frac{1}{\omega_{0,i}} - \frac{\pi}{4}\right)\sin\left(L\int_0^r \frac{N}{r'}\mathrm{d}r'\frac{1}{\omega_{0,j}} - \frac{\pi}{4}\right)\mathrm{d}r. \tag{23}$$

Asymptotically, the inertia of the mode in the g-mode cavity can be written as (e.g. Hekker & Christensen-Dalsgaard 2017)

$$I_g = \frac{A_g^2\pi^2 L}{\omega^3\Delta\Pi} \quad \Leftrightarrow \quad A_g = \sqrt{\frac{\Delta\Pi\,\omega^3 I_g}{L\pi^2}},$$

with $\Delta\Pi = \sqrt{\ell(\ell+1)}\Delta\Pi_\ell$ as the reduced period spacing of the g modes. This yields the following result:

$$\gamma_{c,ij} = \frac{1}{\sqrt{I_{0,i}I_{0,j}}} \int_{g\,\rm cavity} \frac{\Delta\Pi(L^2-1)}{L^2\pi^2}\sqrt{I_{0,g,i}I_{0,g,j}}\frac{N}{2r} \times \left[\cos\left(L\int_0^r \frac{N}{r'}\mathrm{d}r'\frac{\omega_{0,j}-\omega_{0,i}}{\omega_{0,i}\omega_{0,j}}\right) - \sin\left(L\int_0^r \frac{N}{r'}\mathrm{d}r'\frac{\omega_{0,j}+\omega_{0,i}}{\omega_{0,i}\omega_{0,j}}\right)\right]\mathrm{d}r. \tag{24}$$

Here, we have used the trigonometric identity $\sin(a)\sin(b) = \frac{1}{2}(\cos(a-b) - \cos(a+b))$. Using the change of variable[1]

$$s = \int_0^r \frac{N}{r'}\mathrm{d}r' \tag{25}$$

and using the seismic ζ function leads to the following expression:

$$\gamma_{c,ij} = \frac{\Delta\Pi(L^2-1)}{2\pi^2L^2}\sqrt{\zeta_{0,i}\zeta_{0,j}} \times \int_0^{\frac{2\pi^2}{\Delta\Pi}} \cos\left(Ls\frac{\omega_{0,i}-\omega_{0,j}}{\omega_{0,i}\omega_{0,j}}\right) - \sin\left(Ls\frac{\omega_{0,i}+\omega_{0,j}}{\omega_{0,i}\omega_{0,j}}\right)\mathrm{d}s, \tag{26}$$

where we have used the fact that by definition of $\Delta\Pi$, $s(r_{\rm core}) = 2\pi^2/\Delta\Pi$. This was integrated to

$$\gamma_{c,ij} = \frac{\Delta\Pi(L^2-1)}{\pi L^3}\sqrt{\zeta_{0,i}\zeta_{0,j}} \times \left[\frac{\nu_{0,i}\nu_{0,j}}{\nu_{0,j}-\nu_{0,i}}\sin\left(\frac{\pi L}{\Delta\Pi}\frac{\nu_{0,j}-\nu_{0,i}}{\nu_{0,j}\nu_{0,i}}\right) + \frac{\nu_{0,i}\nu_{0,j}}{\nu_{0,j}+\nu_{0,i}}\left(\cos\left(\frac{\pi L}{\Delta\Pi}\frac{\nu_{0,j}+\nu_{0,i}}{\nu_{0,j}\nu_{0,i}}\right) - 1\right)\right], \tag{27}$$

where we have expressed the quantities as a function of the frequency $\nu = \omega/2\pi$ for ease of implementation.

An important point to highlight is that the quantity $\gamma_{c,ij}$, which we derived in this work as part of a new asymptotic formulation including off-diagonal rotational near-degeneracy terms, is expressed using the exact same asymptotic parameters traditionally used in first-order symmetric splitting approaches (i.e. in the characterisation of mixed $\ell = 2$ modes, $\Delta\Pi_2$ replaces $\Delta\Pi_1$ and ζ_2 replaces ζ from the frameworks of Mosser et al. 2012a;

[1] This is possible because in the g-mode cavity, $\frac{N}{r} > 0$, and hence the integral is a strictly increasing function of r. This change of variables leads to $\mathrm{d}s = \frac{N}{r}\mathrm{d}r$.

Goupil et al. 2013; Deheuvels et al. 2014). This shows that we can achieve a better degree of precision on core and envelope rotation measurements by including additional constraints from $\ell = 2$ modes without the need to change the usual formalism and analysis tools.

Our asymptotic formulation in Eq. (27) can be compared with the derivation of Ong et al. (2022) in the $\pi - \gamma$ decoupled mode basis. When the argument of the sin in $\gamma_{c,ij}$ is small, i.e.

$$\frac{\pi L}{\Delta\Pi}\frac{\nu_j - \nu_i}{\nu_j \nu_i} = \pi \frac{P_i - P_j}{\Delta\Pi_\ell} \ll 1, \tag{28}$$

where P_i (resp. P_j) is the period of the mode i (resp j), Eq. (27) becomes equivalent to $\gamma_c \approx \frac{L^2-1}{L^2}\sqrt{\zeta_i\zeta_j}$ when using a first-order Taylor expansion. This gives $\gamma_e \approx -\sqrt{\zeta_i\zeta_j}$. This last approximation yields a result that connects to Eq. (35) of Ong et al. (2022). This situation is most frequent around p-dominated mixed modes. Indeed for two consecutive mixed modes,

$$\frac{\pi L}{\Delta\Pi}\frac{\nu_j - \nu_i}{\nu_j \nu_i} = \frac{\pi}{\Delta\Pi_\ell}\left(\frac{1}{\nu_i} - \frac{1}{\nu_j}\right) \sim \pi\langle\zeta\rangle, \tag{29}$$

where

$$\langle\zeta\rangle = \left(\frac{1}{\nu_i} - \frac{1}{\nu_j}\right)\left(\int_{\frac{1}{\nu_j}}^{\frac{1}{\nu_i}} \frac{\mathrm{d}P}{\zeta(P)}\right)^{-1}, \tag{30}$$

with $P = 1/\nu$ following Mosser et al. (2015) (see their Eq. (12)). Hence, for a small $\langle\zeta\rangle$ (or equivalently a very p-dominated couple of modes), the quantity $\pi\langle\zeta\rangle$ will be small. On the contrary, in the far resonance limit, when

$$\frac{\pi L}{\Delta\Pi}\frac{\nu_j - \nu_i}{\nu_j \nu_i} \gg 1, \tag{31}$$

the non-diagonal terms become negligible compared to the diagonal ones, and we recover symmetrical splittings.

2.3.2. Validation of the new asymptotic formula for near degeneracy effects

To further determine the validity of our new asymptotic formulation of near-degeneracy effects, we sought to reproduce the results of Deheuvels et al. (2017). To do so, we used exactly the same input parameters adopted in their study, only allowing the core and envelope rotation rates to be free (Eq. 17).

To date, KIC 7341231 is the only star in which the near-degeneracy effects of $\ell = 2$ modes have been characterised in detail in one radial order. In their analysis, Deheuvels et al. (2017) adopted a different approach from ours: They computed a 1D stellar model using `Cesam2k` (Morel 1997) while assuming a two-zone rotation profile. They then explicitly computed γ_c from the rotational kernels and solved the full eigenvalue problem. In contrast, our work relies on a fully parametrised asymptotic formulation of γ_c, which allows us to directly compare our results with those obtained from their numerical approach. Specifically, we fitted the core and envelope rotation rates of the two-zone model based on the $\ell = 2$, $m = \pm 2$ rotational splittings obtained from their peakbagging analysis of two $\ell = 2$ multiplets a and b (see their Table 1), together with the $m = 0$ mode frequencies ($\nu_{0,a}$ and $\nu_{0,b}$) and the corresponding trapping fractions ζ_a and ζ_b reported in their Table 3. To compute the $m = \pm 2$ components of each mixed a and b, we evaluated the eigenvalues of the following matrix, as done by Deheuvels et al. (2017) in their Appendix A:

$$\begin{bmatrix} \nu_{0,a}^2 + 2\nu_{0,a}\dfrac{\langle \boldsymbol{\delta r}_{0,a}, \hat{\mathcal{L}}_{\mathrm{rot},m}\boldsymbol{\delta r}_{0,a}\rangle}{2\pi I_{0,a}} & 2\nu_{0,a}\dfrac{\langle \boldsymbol{\delta r}_{0,a}, \hat{\mathcal{L}}_{\mathrm{rot},m}\boldsymbol{\delta r}_{0,b}\rangle}{2\pi\sqrt{I_{0,a}I_{0,b}}} \\ 2\nu_{0,b}\dfrac{\langle \boldsymbol{\delta r}_{0,b}, \hat{\mathcal{L}}_{\mathrm{rot},m}\boldsymbol{\delta r}_{0,a}\rangle}{2\pi\sqrt{I_{0,a}I_{0,b}}} & \nu_{0,b}^2 + 2\nu_{0,b}\dfrac{\langle \boldsymbol{\delta r}_{0,b}, \hat{\mathcal{L}}_{\mathrm{rot},m}\boldsymbol{\delta r}_{0,b}\rangle}{2\pi I_{0,b}} \end{bmatrix}. \tag{32}$$

This formulation is an approximation of (9) introduced by Deheuvels et al. (2017). Since they use this approximated form in their article, we choose to do the same when vetting our results in order to stay as close to the article as possible. This is the only part of the present work in which we compute the splittings due to near-degeneracy effects with this approximation; in the rest of our work, we solve the full quadratic eigenvalue problem (9).

In our formulation, the off-diagonal elements of this matrix were computed using Eq. (27), while the diagonal terms were derived from Eq. (16) (Goupil et al. 2013; Deheuvels et al. 2014).

The values and uncertainties on the inferred core and envelope rotation rates were estimated using a Monte Carlo approach. The resulting values are shown in Fig. B.1. Using identical mixed-mode parameters but replacing their numerical model with our asymptotic formulation, we achieved an excellent agreement with the published results. We obtained $\Omega_{\mathrm{core}}/2\pi = 772 \pm 9$ nHz and $\Omega_{\mathrm{env}}/2\pi = 45 \pm 6$ nHz, while Deheuvels et al. (2017) reported $\Omega_{\mathrm{core}}/2\pi = 771 \pm 13$ nHz and $\Omega_{\mathrm{env}}/2\pi = 45 \pm 12$ nHz. The close agreement between the two methods confirms that the asymptotic formulation provides a robust and accurate description of the observed rotational splittings and can be used to analyse asteroseismic observations of $\ell = 2$ modes without the need of numerical models. Our fitted measurement also hints at our approach being able to obtain better precision, which we confirm in Section 4.

3. Data analysis framework

Our next aim was to apply the asymptotic formalism described by Eqs. (16), (17) and (27) in order to perform global fits of the PSD, thereby constraining the mixed-mode parameters and the core as well as envelope rotation rates while using all available data. In particular, we deliberately avoided performing peakbagging prior to the model fitting, as whether a given peak represents a genuine oscillation mode or merely stochastic noise can often be ambiguous. The main advantage of fitting the PSD directly with a physically informed model based on asymptotic relations is that the distinction between signal and noise naturally emerges from the fit itself without requiring any subjective preselection of peaks.

To accomplish this, we employed a Markov chain Monte Carlo approach within a Bayesian framework to fit the oscillation modes in the PSD. The p- and mixed-mode patterns were created using the `sloscillations` code developed in Kuszlewicz et al. (2019, 2023), which was extended to incorporate the near-degeneracy effects based on Section 2. How the synthetic PSD was generated is described in Sect. 3.1 below.

3.1. Synthetic power spectral density

3.1.1. Description of the set-up of the asymptotic model

The asymptotic model used in the fitting procedure predicts the full oscillation spectrum from a set of physically motivated parameters. For each angular degree $\ell \in \{0, 1, 2\}$, the model

generates the underlying p- and g-mode frequencies from the asymptotic relations described below, which are then coupled through the mixed-mode formalism and corrected for rotational splitting at first order (for $\ell = 1$) or through the full quadratic eigenvalue problem (for $\ell = 2$).

The free parameters of the model therefore include the global p-mode pattern parameters ($\Delta\nu$, ε, $\delta\nu_{0,\ell}$, α, $\beta_{0,\ell}$); the g-mode period-spacing and phase parameters ($\Delta\Pi_\ell$, $\varepsilon_{g,\ell}$); the p–g coupling strengths (q_ℓ); and the core and envelope rotation rates ($\Omega_{\rm core}$, $\Omega_{\rm env}$) as well as the stellar inclination angle ($\theta_{\rm inc}$).

Each predicted mode is assigned a Lorentzian profile with an analytically prescribed linewidth and height, and these components are summed together with a synthetic granulation and white-noise background to produce a fully specified model of the PSD.

3.1.2. Pure pressure and gravity modes

The pure p modes were computed using the following equation (e.g. Tassoul 1980; Elsworth et al. 1990; Mosser et al. 2011; Lund et al. 2017; Breton et al. 2022):

$$\nu_{\mathrm{p;n},\ell} = \left(n + \frac{\ell}{2} + \varepsilon + \beta_{0,\ell}(n - n_{\max}) + \frac{\alpha}{2}(n - n_{\max})^2\right)\Delta\nu - \delta\nu_{0,\ell}, \tag{33}$$

where $n_{\max}$ is the order of the mode of maximum power, ε is the global p-mode phase shift, and $\delta\nu_{0,\ell}$ is the frequency shift of the modes from their first order asymptotic position (Tassoul 1980). To capture the frequency dependence of $\Delta\nu$ and $\delta\nu_{0,\ell}$, α and $\beta_{0,\ell}$ are introduced ad hoc (Elsworth et al. 1990; Lund et al. 2017; Breton et al. 2022). The pure g modes were computed using (e.g. Tassoul 1980)

$$\nu_{\mathrm{g;n},\ell} = \frac{1}{\Delta\Pi_\ell(n + \frac{1}{2} + \varepsilon_{\rm g})}, \tag{34}$$

where $\varepsilon_{\rm g}$ is the phase shift of the g modes.

3.1.3. Mixed modes with rotation

Unperturbed mixed-mode frequencies were computed using the following equation (Shibahashi 1979):

$$\mathrm{cotan}\,(\Theta_{\rm g})\tan(\Theta_{\rm p}) = q_\ell \tag{35}$$

with (Ong & Gehan 2023)

$$\Theta_{\rm p} = \frac{\pi}{\Delta\nu}\left(\nu - \nu_{\rm p}\right),$$
$$\Theta_{\rm g} = \frac{\pi}{2} - \frac{\pi}{\Delta\Pi_\ell}\left(\frac{1}{\nu_{\rm g}} - \frac{1}{\nu}\right), \tag{36}$$

and where q_ℓ is the coupling factor between the p- and g- modes for the corresponding order ℓ (we expect $q_2 < q_1$ due to the shallower p-mode cavity for $\ell = 2$ modes).

We introduced the effects of rotation on the unperturbed frequencies at the first perturbative order for the $\ell = 1$ components and solved the full rotating quadratic eigenvalue problem Eq. (9) with asymptotic matrix elements for $\ell = 2$ (based on our asymptotic formulation Eq. (27)) modes using the `slepc4py` (Hernandez et al. 2005; Dalcin et al. 2011) Python library.

When computing the off diagonal elements of the rotation matrix, we used the asymptotic formula for ζ defined in Eq. (15) such that (Goupil et al. 2013; Deheuvels et al. 2015; Hekker & Christensen-Dalsgaard 2017)

$$\zeta(\nu) = \left[1 + \frac{\nu^2\Delta\Pi_\ell}{\Delta\nu}\frac{1}{q\cos^2(\Theta_p) + \frac{1}{q}\sin^2(\Theta_p)}\right]^{-1} \tag{37}$$

while using the above definition of Θ_p.

3.1.4. Modelling the linewidths, amplitudes, and heights of the modes

This paragraph describes the equations and methodologies used to compute the linewidths, amplitudes, and heights of the modes in the `sloscillations` code by Kuszlewicz et al. (2019) for the sake of completeness and clarity. These parameters were fully derived from scaling relations and analytical expressions and are thus not fitted parameters in the model. We adopted effective-temperature-dependent scaling relations for the p-mode linewidths, parametrised as a function of temperature, following the empirical prescriptions of Corsaro et al. (2012), Lund et al. (2017). The radial-mode amplitudes follow a Gaussian envelope centred on $\nu_{\max}$, with width tied to the envelope full width at half maximum and a peak amplitude that scales with global parameters ($\nu_{\max}$, $\Delta\nu$). The per-degree amplitudes were set by standard photometric visibilities as in Kuszlewicz et al. (2019) and, for non-radial multiplets, by geometric inclination ($\theta_{\rm inc}$) factors (Gizon & Solanki 2003). For mixed $\ell = 1$ and $\ell = 2$ modes, we modulated the nominal p-mode amplitudes by $(1-\zeta)^{\frac{1}{2}}$ (Mosser et al. 2018; Basu & Chaplin 2017). The mode heights in the power spectrum were computed from the time-domain amplitudes and the linewidths using the finite-observation-length correction of Fletcher et al. (2006). For mixed modes, we used the mixed-mode generalisation that explicitly includes the inertia ratio ζ (Basu & Chaplin 2017), ensuring that g-dominated mixed modes appear with an appropriately reduced height at a fixed amplitude. Each mode contributes a Lorentzian profile to the PSD, centred at the asymptotic frequency and with the height and width described above.

The background of the synthetic PSD was modelled with the usual super-Lorentzian granulation components and white noise (e.g Kallinger et al. 2014). It was generated in the time domain via a Gaussian-process representation of convection and granulation following Kuszlewicz et al. (2019), where a kernel encapsulates the covariance of stochastic surface motions (e.g. Foreman-Mackey et al. 2017; Pereira et al. 2019; O'Sullivan & Aigrain 2024). This data was Fourier transformed, and the resulting PSD provided the granulation floor plus white noise that forms the background in the PSD. On top of this background, the oscillation spectrum was added, producing a self-consistent synthetic PSD where both the convective noise and p-mode power originate from the same underlying time-domain process. During the fitting procedure, the synthetic background was then normalised using the same procedure applied to the observed data (see Sect. 4.1). Since the same background normalisation was applied consistently to both the observed and synthetic spectra, the fit remained statistically self-consistent and did not introduce any bias in the inferred mode frequencies.

3.2. Description of the Bayesian fitting procedure

3.2.1. Priors on p modes and $\ell = 1$ mixed modes

Appendix C describes the method used to define prior ranges for the rotational, p-mode, and $\ell = 1$ mixed-mode parameters. These

ranges are guided by both theoretical expectations and previous observational studies.

3.2.2. Priors on the $\ell = 2$ period spacing $\Delta\Pi_2$ and phase $\varepsilon_{g,2}$

Using the fact that the period spacing $\Delta\Pi = L\Delta\Pi_\ell$ is constant (Tassoul 1980), we obtained

$$\Delta\Pi_2 = \frac{\Delta\Pi_1}{\sqrt{3}}. \tag{38}$$

Hence, once we had measured $\Delta\Pi_1$, we chose to assign a flat prior within ±5% of the value of $\Delta\Pi_2$ from Eq. (38).

As for $\varepsilon_{g,2}$, we have, to our knowledge, no theoretical grounds to constrain it. Hence, we chose to use an uninformative flat prior between zero and one, as done for $\varepsilon_{g,1}$ (see Appendix C).

3.2.3. Priors on the $\ell = 2$ modes coupling parameter q_2

We examined what constraints could be put on q_2, the coupling factor of $\ell = 2$ modes, depending on the inclination angle of the star compared to the line of sight ($\theta_{\rm inc}$), which we estimated by the preliminary fit of the $\ell = 1$ modes (Appendix C). When the $\ell = 2$, $m = 0$ modes are visible, we used the technique described in Sect. 3.2.4. When the angle of inclination makes the $\ell = 2$ and $m = 0$ modes not visible, we used the result of Sect. 3.2.5.

3.2.4. Priors on the $\ell = 2$ modes coupling parameter q_2 using the $m = 0$ modes

Using Eq. (15) of Ong & Gehan (2023), we obtained that for two consecutive mixed modes (with the same ℓ order) of frequency ν_a and ν_b,

$$\begin{aligned}&\arctan\left(\frac{\tan\left(\Theta_{\mathrm{p},a}\right)}{q_\ell}\right) - \arctan\left(\frac{\tan\left(\Theta_{\mathrm{p},b}\right)}{q_\ell}\right)\\ &= \frac{\pi}{\Delta\Pi_\ell}\left(\frac{1}{\nu_a} - \frac{1}{\nu_b} + \Delta\Pi_\ell\right).\end{aligned} \tag{39}$$

Using trigonometric relations, we show that this formula is equivalent to

$$\begin{aligned}&\frac{\tan\left(\Theta_{\mathrm{p},a}\right) - \tan\left(\Theta_{\mathrm{p},b}\right)}{q_\ell}\frac{1}{1 + \frac{1}{q_\ell^2}\tan\left(\Theta_{\mathrm{p},a}\right)\tan\left(\Theta_{\mathrm{p},b}\right)}\\ &= -\tan\left(\frac{\pi}{\Delta\Pi_\ell}\left(\frac{1}{\nu_b} - \frac{1}{\nu_a}\right)\right),\end{aligned} \tag{40}$$

which is conveniently a second-order polynomial in $\frac{1}{q_\ell}$.

Hence, by defining

$$\begin{aligned}K &= \tan\left(\frac{\pi}{\Delta\Pi_\ell}\left(\frac{1}{\nu_b} - \frac{1}{\nu_a}\right)\right)\\ A &= K\tan\left(\Theta_{\mathrm{p},a}\right)\tan\left(\Theta_{\mathrm{p},b}\right)\\ B &= \tan\left(\Theta_{\mathrm{p},b}\right) - \tan\left(\Theta_{\mathrm{p},a}\right)\\ \Delta &= B^2 - 4AK,\end{aligned} \tag{41}$$

we obtained that q_ℓ is given by

$$q_\ell = \frac{2A}{B + \sqrt{\Delta}}. \tag{42}$$

In order to obtain q_2, we thus needed $\Delta\Pi_2$, $\Delta\nu$, ν_a, ν_b, and the position of the $\ell = 2$ p mode that is obtained from the radial mode frequency and $\delta\nu_{0,2}$.

3.2.5. Priors on the $\ell = 2$ modes coupling parameter q_2 using the $\ell = 1$ mode coupling parameter q_1

When the inclination angle of the rotation axis is such that the $m = 0$ components of the multiplet splittings are not visible, we cannot use the above method to yield an estimate of q_2. Indeed the previous method relies on the frequencies of the pure mixed modes not affected by dynamical processes, which is not the case for the components of a multiplet with $|m| > 0$. Hence, we derived an upper bound of q_2 as a function of q_1. In order to do so, we used the approximation that in the evanescent zone, $N \ll \omega \ll S_\ell$, where N is the Brunt-Väisälä frequency and S_ℓ the Lamb frequency. In the approximation of a thick evanescent zone, the transmission coefficient can be approximated as (Unno et al. 1989; Takata 2016a)

$$t_{\ell,\mathrm{thick}} \approx \left(\frac{r_0}{r_\ell}\right)^L, \tag{43}$$

where r_0 is the turning point between the g-mode cavity and the evanescent zone, which is independent of ℓ, and r_ℓ is the turning point at the limit between the evanescent zone and the p-mode cavity.

While this thick evanescent zone approximation may not be applicable to $\ell = 1$ modes, we know from Takata (2016b) that $t_{\ell,\mathrm{thick}} > t_{\ell,\mathrm{thin}}$, where $t_{\ell,\mathrm{thin}}$ is the transmission coefficient computed with the asymptotic equation that is appropriate when the evanescent zone is thin (Takata 2016b; van Lier et al. 2025). Hence, this approximation is appropriate in the search of an upper boundary on q_2. At fixed frequency, the monotonic increase of S_ℓ with ℓ implies $r_2 > r_1$ and therefore

$$t_2 \approx \left(\frac{r_0}{r_2}\right)^{\sqrt{6}} < \left(\frac{r_0}{r_1}\right)^{\sqrt{6}} \approx t_1^{\sqrt{3}}. \tag{44}$$

Using the fact that (Takata 2016a)

$$q_\ell = \frac{1 - \sqrt{1 - t_\ell^2}}{1 + \sqrt{1 - t_\ell^2}}, \tag{45}$$

We finally obtain

$$q_2 < \frac{1 - \sqrt{1 - \left(\frac{4q_1}{(q_1+1)^2}\right)^{\sqrt{3}}}}{1 + \sqrt{1 - \left(\frac{4q_1}{(q_1+1)^2}\right)^{\sqrt{3}}}}. \tag{46}$$

3.2.6. Likelihood adopted in the Markov chain Monte Carlo approach

In our Markov chain Monte Carlo approach, we adopted the likelihood appropriate for a power spectrum whose noise follows a χ^2 distribution with two degrees of freedom (Woodard 1984; Toutain & Appourchaux 1994; Breton et al. 2022). The corresponding log-likelihood is

$$\ln\mathcal{L} = -\sum_i\left[\frac{P_i}{M_i} + \ln M_i\right],$$

where P_i denotes the observed power and M_i is the model power at a frequency bin i. The Bayesian inference procedure then adjusts the asymptotic parameters so as to maximise this likelihood, thereby ensuring that the resulting synthetic PSD matches the observed one as closely as possible. The different components of the model are presented in the paragraphs above.

3.2.7. Adopted fitting strategy

In order to fit the asymptotic pattern to asteroseismic data, we used a three-step approach. (i) In order to find priors on pressure mode parameters, we ran the global asteroseismic code PyA2Z (Liagre et al., in prep., based on the A2Z code Mathur et al. 2010), which gives guesses of the large frequency separation, $\Delta\nu$; the frequency of maximum power, $\nu_{\rm max}$; and the p-mode phase shift, ε (as well as the period spacing, $\Delta\Pi_1$, of $\ell = 1$ g modes). (ii) We fitted the radial mode pattern and the first order split $\ell = 1$ mixed-mode pattern following Sect. C.1 (i.e. we fitted $\Delta\nu, \varepsilon, \delta\nu_{0,1}, \alpha, \Delta\Pi_1, q_1, \varepsilon_{g,1}, \Omega_{\rm core}, \Omega_{\rm env}, \beta_{0,1}$, and $\theta_{\rm inc}$, which is the inclination angle of the rotation axis compared to the line of sight for KIC 8179973) to get the parameters needed to obtain priors on $\ell = 2$ modes from Eqs. (38), (42), and (46). (iii) Once we had the priors on all parameters (listed in Table C.1), we performed the global asymptotic fit of the PSD ($\ell = 0, 1, 2$ modes with rotation) following Appendices C.2 and C.3. We chose not to include $\ell \geq 3$ modes in our model, as their amplitudes are very small.

While the mixed $\ell = 1$ mode parameters and pressure mode parameters were already fitted in the first two steps of the procedure, we chose not to freeze them during the global fit to avoid biases in the inferred rotational and $l = 2$ parameters. This resulted in a global fit, the corner plot of which can be found in Appendix C.4.

4. The first asymptotic fits of near-degeneracy effects in quadrupolar mixed modes

4.1. Selection of candidates and data pre-processing

The first target we used to validate this new asymptotic formulation of asymmetric rotational splitting is the one studied with a numerical modelling approach by Deheuvels et al. (2017): KIC 7341231. In order to find additional targets with mixed $\ell = 2$ modes on which to apply our formulation of asymmetric rotational splittings, we chose to focus on stars in the early red giant or late sub-giant evolutionary stage, as they are expected to exhibit higher coupling factors for both $\ell = 1$ and $\ell = 2$ modes than more evolved stars. A convenient sample for exploring this evolutionary phase is in Liagre et al. (2025), who re-analysed aliased asteroseismic data from ≈2000 long cadence *Kepler* light curves and found a new sample of ≈350 young red giants with $\nu_{\rm max}$ above or close to the Nyquist frequency of the *Kepler* long cadence data. While the sample presented in Liagre et al. (2025) contains more than 300 stars with pulsations above the Nyquist frequency and hence in the early red giant evolutionary stage, we wanted to analyse stars with a short-cadence timeseries to avoid misinterpreting aliased peaks as modes and with sufficient resolution and a signal-to-noise ratio to work well with our fitting procedure. This significantly reduced the available number of targets, and among those, we found that KIC 8179973 was the most promising, as a visual inspection of the echelle diagram of the star showed clear $\ell = 2$ avoided crossings. We therefore selected KIC 8179973 as another good candidate for a global fit of $\ell = 1, 2$ mixed modes including near-degeneracy effects, as it exhibits mixed $\ell = 2$ modes with an exceptional signal-to-noise ratio.

The seismic analyses were done using short-cadence *Kepler* light curves filtered at 20 days and were obtained from the Mikulski Archive for Space Telescopes (MAST) archive. They were corrected with the *Kepler* Asteroseismic Data Analysis and Calibration Software (`KADACS`; García et al. 2011) to remove outliers, correct any jumps and drifts, and stitch together the quarters. All the observational gaps were interpolated using inpainting techniques based on a multi-scale discrete cosine transform (García et al. 2014; Pires et al. 2015). We isolated the oscillatory signal in the PSD from the granulation background, which dominates the PSD at frequencies around $\nu_{\rm max}$. We implemented the background normalisation procedure using the empirical scaling relation established in Mosser et al. (2012b):

$$\mathrm{PSD\,(SNR)} = \frac{P}{\left(\nu_{\rm max}^{-2.41}\right)\left(\frac{\nu}{\nu_{\rm max}}\right)^{-2.1} 6.37 \times 10^6}, \tag{47}$$

where P represents either the observed or the synthetic power spectrum density. This normalisation effectively flattens the granulation background while preserving the relative amplitudes of the oscillation modes. Subsequently, we isolated the region of interest around $\nu_{\rm max}$ (the extracted frequency window spans $\nu_{\rm max} - 3\Delta\nu \leq \nu_{\rm max} \leq \nu_{\rm max} + 4\Delta\nu$).

4.2. Results of the Bayesian asymptotic fitting

Figures 2 and 3 show the results of the fitting procedure described in Section 3 obtained for the two stars. The results are also reported in Table 1 along with the 1σ uncertainties extracted from the Bayesian analysis (the corner plots of the final fits can be found in Appendix C.4). When the posterior was asymmetrical, we chose to report the highest value of uncertainty as the error bar.

4.2.1. KIC 7341231

In Figure 2, we show our global fit of the mixed modes of KIC 7341231 and highlight in panels b and c the identification of $\ell = 2$ modes on two consecutive radial orders. We vetted the asymptotic formula and fitting framework by comparing the results with the work of Deheuvels et al. (2017), which made use of complete evolutionary models of the star to analyse the radial order represented in panel b. We show that our fit is consistent with all visible $\ell = 2$ modes in the PSD, as first identified in Fig. 1 of Deheuvels et al. (2017) in the neighbourhood of 380 μHz.

Apart from the specific radial order analysed by Deheuvels et al. (2017) in the vicinity of 380 μHz, the asymptotic fit allows for systematic identification of $\ell = 2$ modes across the four surrounding radial orders (see Fig. C.4), which is a first for this star. In addition, we were able to properly identify multiplet components even when modes overlap between different angular degrees (ℓ). For instance, in Fig. 2 panels a and c, around 413 μHz, three modes of degree $\ell = 0, 1, 2$ are superimposed, and each peak has been successfully identified individually through reconstruction of the asymptotic mode pattern.

In Table 2, we show that our estimate of core and envelope rotation rates are in agreement with model-based measurements from Deheuvels et al. (2017) and consistent across radial orders. We obtained about three times smaller uncertainties for the core rotation rate and two times smaller for the envelope rotation rate.

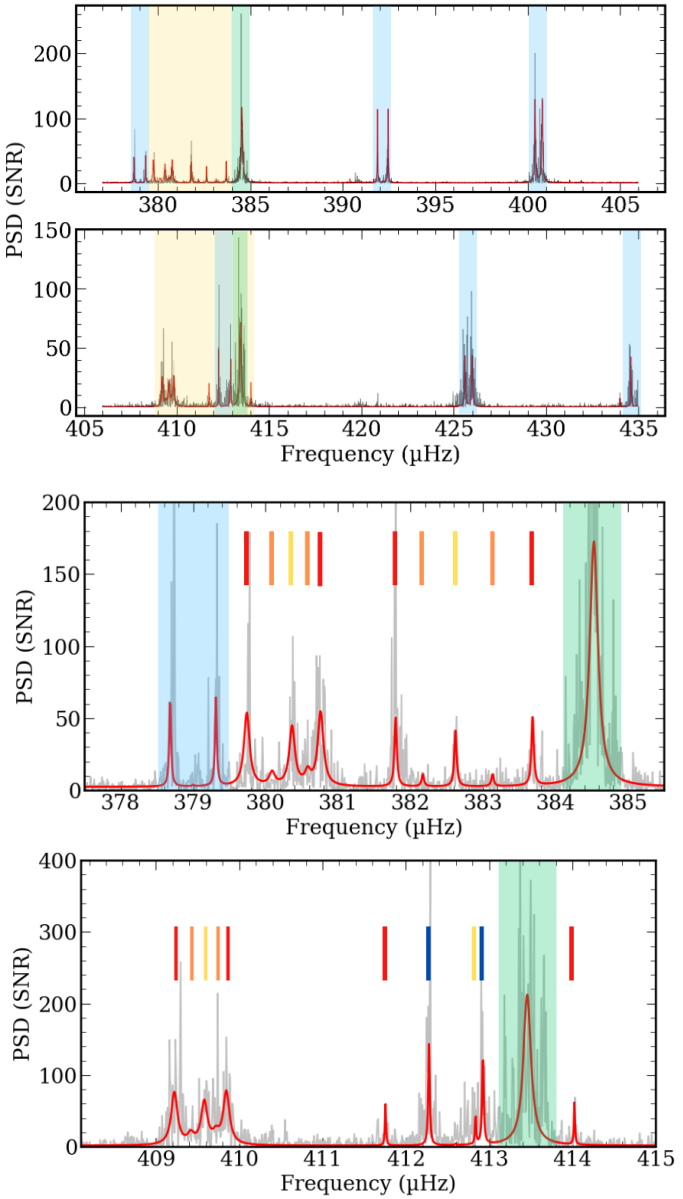

Fig. 2. Asymptotic fit of KIC 7341231. In both panels, the *Kepler* data are in grey, and our asymptotic fit is in red. The radial, $\ell = 1$, and $\ell = 2$ modes are highlighted by the shading in green, blue, and yellow, respectively. Panel a: Two orders showing mixed $\ell = 2$ modes with asymmetric splittings. Panel b: Zoom near 411 μHz on split $\ell = 2$ modes. The $m = 0$, ±1, and ±2 components are marked in yellow, orange, and red. Panel c: Zoom near 381 μHz on split $\ell = 2$ modes. The model is shown with thick red lins, data are in grey. The $m = 0$, ±1, and ±2 components of the $\ell = 2$ mode are marked in yellow, orange, and red, and the $m = \pm1$ components of the $\ell = 1$ mode are marked in dark blue.

This is due to the fact that our fit is global (as also performed for magnetic effects in Hatt et al. 2024). Indeed, uncertainties in mixed-mode parameters are usually estimated through non-parametric methods that do not exploit the full spectral information and instead consider errors on individual frequencies rather than the coherence of the global mixed-mode pattern (e.g. Gehan et al. 2018; Kuszlewicz et al. 2023). The global Bayesian fit also delivers better precision on asymptotic parameters in Table 1. For this reason, we advocate for broad use of these global fitting methods.

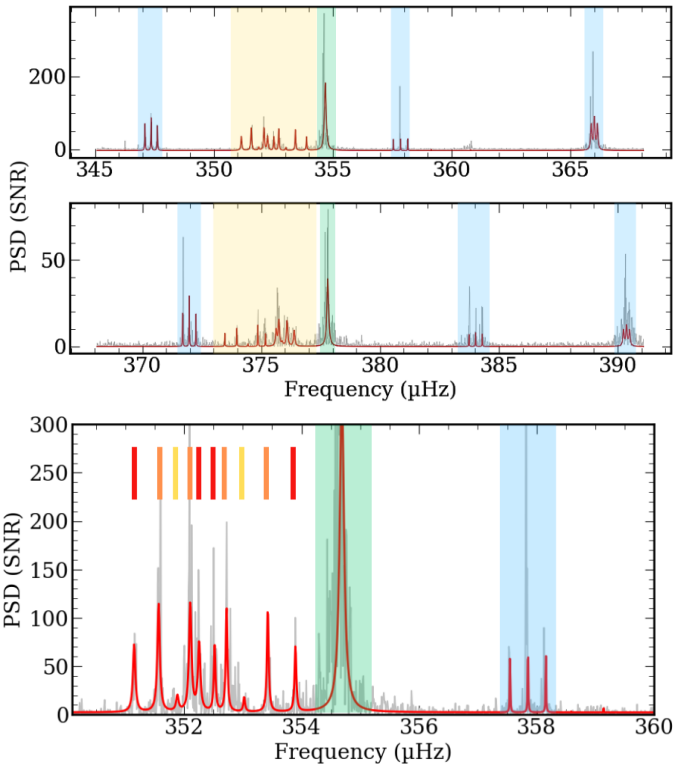

Fig. 3. Asymptotic fit of KIC 8179973. In both panels, the *Kepler* data are in grey, and our asymptotic fit is in red. The radial, $\ell = 1$, and $\ell = 2$ modes are highlighted by the shading in green, blue, and yellow, respectively. Panel a: Two orders showing mixed $\ell = 2$ modes with asymmetric splittings. Panel b: Zoom near 352 μHz on split near-degenerate $\ell = 2$ modes. The quadrupolar mixed $m = 0$, ±1, and ±2 components are marked in yellow, orange, and red, respectively. The full fit can be found in Fig. C.7.

In order to assess the gain from adding constraints from $\ell = 2$ modes to the fitting procedure, we estimated the Bayesian information criterion (BIC; Schwarz 1978) by comparing the fit performed with $\ell = 2$ mixed modes and $\ell = 2$ p modes only. To that end, we fitted the data again with split mixed dipole modes and pressure $\ell = 2$ modes as usually done in the community and compared that restricted model against the full fit of the present work. The inclusion of mixed $\ell = 2$ modes in the model leads to a BIC that is 3726 points lower than when using only mixed $\ell = 1$ modes and pressure $\ell = 2$ modes on the target KIC 7341231. Because the differences in the BIC approximate

$$\Delta\mathrm{BIC} \approx -2\ln(\mathrm{BF}), \tag{48}$$

where BF is the bayes factor, such a large ΔBIC corresponds to overwhelmingly strong statistical evidence in favour of the extended model. We do not report the absolute BIC values themselves, as they are not tied to any absolute scale and carry no stand-alone interpretation. Only their differences have statistical meaning for model comparison. This substantial improvement in BIC therefore indicates very strong support for including the mixed $\ell = 2$ modes, suggesting that the extended model provides a significantly better representation of the observed oscillation data. As a result, the physical inferences drawn from this model (such as internal rotation rates) can be considered significantly more robust and better constrained than those inferred from mixed $\ell = 1$ modes only.

Table 1. Best-fit parameters for KIC 7341231 and KIC 8179973 with 1σ uncertainties.

Param. \ Star	KIC 7341231	KIC 8179973
$\nu_{\max}$ (μHz)	408 ± 15	347 ± 12
$\Delta\nu$ (μHz)	29.00 ± 0.01	23.00 ± 0.01
ε	0.256 ± 0.004	0.425 ± 0.006
$\delta\nu_{0,1}$ (μHz)	−0.118 ± 0.02	−0.346 ± 0.016
$\delta\nu_{0,2}$ (μHz)	3.413 ± 0.021	2.182 ± 0.025
$\beta_{0,2}$	0.009 ± 0.001	0.011 ± 0.001
$\Delta\Pi_1$ (s)	111.180 ± 0.025	97.011 ± 0.008
q_1	0.379 ± 0.001	0.197 ± 0.001
$\varepsilon_{g,1}$	0.310 ± 0.006	0.279 ± 0.003
$\Delta\Pi_2$ (s)	64.422 ± 0.007	56.015 ± 0.023
q_2	0.040 ± 0.001	0.020 ± 0.001
$\varepsilon_{g,2}$	0.138 ± 0.004	0.135 ± 0.02
$\Omega_{\rm core}/2\pi$ (nHz)	781 ± 4	672 ± 8
$\Omega_{\rm env}/2\pi$ (nHz)	53 ± 6	49 ± 8
$\theta_{\rm inc}$ (°)	85 (fixed)	51 ± 3
α	0.009 ± 0.001	0.006 ± 0.001
$\beta_{0,1}$	0.008 ± 0.001	0.004 ± 0.001

Table 2. Comparison of the rotation rates found in this work and Deheuvels et al. (2017, Dh17 in the table).

Parameter		This work	Dh17
$\Omega_{\rm core}/2\pi$	(nHz)	781 ± 4	771 ± 13
$\Omega_{\rm env}/2\pi$	(nHz)	53 ± 6	45 ± 12

4.2.2. KIC 8179973

We performed the first fit of the radial and $\ell = 1, 2$ mixed-mode pattern for KIC 8179973. This star presents a particularly asymmetric pattern in the $\ell = 2$ regions, as the multiplets are very close to each other (see panels a and b of Fig. 3). The asymptotic prescription (Eq. 27) yields a very good interpretation of the PSD, with all visible modes being accurately represented (see also Fig. C.7). The values of $\Delta\Pi_1$, $\varepsilon_{g,1}$, and q_1 are also in the range of the expected values from scaling relations and measurements of Mosser et al. (2017a), Kuszlewicz et al. (2023). The small number of visible mixed $\ell = 2$ modes is expected based on the small mixed-mode density parameter (Gehan et al. 2018) $\mathcal{N}_2 = \Delta\nu/(\Delta\Pi_2\nu_{\max}^2) \approx 3.4$ and the fact that the coupling factor (q_2) is very small. Furthermore, for this star, we used a much less informative prior for q_2, as in the fit of KIC 7341231, which shows the robustness of our fitting method. In addition, $\Delta\Pi_2$ and $\Delta\Pi_1$ are compatible within 2σ following Eq. (38). From the global fit, we obtained $\Omega_{\rm core} = 671 \pm 8\,\mu$Hz and $\Omega_{\rm env} = 49 \pm 8\,\mu$Hz, which are within the expected range for a young red giant star (Gehan et al. 2018).

As for KIC 7341231, the uncertainties we obtained on KIC 8179973 are significantly smaller than those typically reported in similar studies (see e.g. Gehan et al. 2018; Deheuvels et al. 2014). This improvement highlights the strength of our global fitting procedure, which (i) minimises the uncertainties by simultaneously exploiting information from multiple modes and (ii) naturally mitigates the ambiguity between noise and genuine power excesses thanks to the intrinsic pattern constraints of the analysis. Compared to a fit that includes only the pure $\ell = 2$ p modes, the BIC derived from the full asymptotic framework is lower by 3185 points. This provides strong statistical evidence that the prescription including mixed quadrupole modes and incorporating near-degeneracy effects offers a superior inference of the underlying physical parameters. This measurement of near-degeneracy effects in a second early red giant paves the way for a fully automated fitting pipeline based on asymptotic mixed-mode parameters across ℓ.

5. Conclusions

This work is the first to infer the complete set of asymptotic parameters of $\ell = 2$ modes and the first to provide a fit of $\ell = 2$ mode near-degeneracy splittings while not relying on a numerical model of the structure of a star. In particular, it has led to the first inferences of q_2, $\Delta\Pi_2$, and $\varepsilon_{g,2}$, and with custom ways to constrain the coupling factor q_2, our work paves the way for an automation of the fit and identification of $\ell = 2$ mixed modes.

Our results for $\Delta\Pi_1$ and $\Delta\Pi_2$ in KIC 8179973 are consistent within 2σ. However, in KIC 7341231, the values agree within a few tenths of a second with non-overlapping errors, suggesting either a small deviation from the asymptotic theory or the influence of surface effects that were not fully accounted for in this work. Indeed, because the fit of asymptotic mixed modes is very reliant on the position of the pure p-mode, a difference in the surface effects affecting the $\ell = 1$ and $\ell = 2$ notional p modes would suffice to explain a small difference in $\Delta\Pi$. In addition, our asymptotic formulation, including the $\ell = 2$ modes, enabled us to put stronger constraints on the rotation rates of our targets. Indeed, in KIC 7341231 we measured an envelope (resp. core) rotation rate of 57 ± 11 nHz (resp. 777 ± 10 nHz) with only $\ell = 1$ modes, while with the addition of $\ell = 2$ modes combined with a global fitting framework, we obtained an envelope (resp. core) rotation of 53 ± 6 nHz (resp. 781 ± 4 nHz). Those values are compatible with each other, and we also observed that the inclusion of the mixed $\ell = 2$ modes makes the uncertainty drop by a factor approximately equal to two (2.5 for the core rotation and 1.8 for envelope rotation). This is mostly due to the inclusion of more modes in the fitting procedure. There might also be a different contribution from the sensitivity kernels of the $\ell = 2$ modes. Specifically, their shallower turning points offer distinct constraints from those of $\ell = 1$ modes in the p-mode cavity, suggesting a potential for improved radial resolution in future inversions. This strengthening of the constraints on rotation rates is further supported by the fact that including the mixed $\ell = 2$ modes made the BIC of the fit of KIC 7341231 and KIC 8179973 drop by more than 3000 points, which is strong statistical evidence that the use of the new formulation allowing a fit of $\ell = 2$ mixed modes leads to a better physical inference. In addition, as we have shown in Fig. 2, our fitting framework can distinguish between entwined split modes of different ℓ, which shows the robustness of the fitting methodology.

The asymptotic framework is also expected to simplify future studies of magnetic signatures and yield new results using not only the $\ell = 1$ but also the $\ell = 2$ modes to characterise magnetic fields in the RGB. We expect that the measurement of q_2 will help constrain the mode suppression phenomenon (e.g. Fuller et al. 2015; Stello et al. 2016a; Mosser et al. 2017b) for $\ell = 2$ modes (Stello et al. 2016b), as the loss in power of weakened non-radial modes is expected to be linked to the transmission coefficient from the p-mode cavity to the g-mode cavity (Fuller et al. 2015; Loi 2020a; Müller et al. 2025). Low and radial-order-dependent values of $\Delta\Pi_2$ should serve as a hint of the presence of an internal magnetic field, as is the case for $\Delta\Pi_1$

(Loi 2020b; Bugnet 2022; Deheuvels et al. 2023). In a follow-up study (Liagre et al., in prep.), we will employ this new formulation and framework together with first-order magnetic effects (e.g. Gomes & Lopes 2020; Bugnet et al. 2021; Mathis et al. 2021; Bugnet 2022; Li et al. 2022; Mathis & Bugnet 2023; Bhattacharya et al. 2024; Das et al. 2024; Li et al. 2023; Hatt et al. 2024; Bhattacharya et al. 2024) in order to disentangle rotation-induced near-degeneracy asymmetries from magnetic ones in $\ell = 2$ modes. This is particularly important, as it should provide stronger constraints on the magnetic field topology, as shown by Das et al. (2024).

We anticipate that ongoing and upcoming space missions will continue to expand the sample of stars with good signal-to-noise ratios observed in this intermediate evolutionary phase. During its extended operations, the Transit Exoplanet Survey Satellite (TESS; Ricker et al. 2014) mission improved its temporal resolution, reducing the full-frame image cadence first to 10 minutes and later to 3 minutes. The TESS data are currently being calibrated for seismology (García et al. 2024, and in prep.), which will enable large-scale and homogeneous seismic analyses. Moreover, the upcoming PLAnetary Transits and Oscillations of stars (Rauer et al. 2014) mission is expected to enable the detection of a large number of solar-like oscillators in the sub-giant and early giant phases from the calibration sample, and recent yield predictions are consistent with this expectation (Goupil et al. 2024). Using this global asymptotic description along with the Bayesian fitting framework, we expect to not only characterise the rotation profile of stars exhibiting mixed $\ell = 2$ modes with increased precision but also the rotation profiles of more evolved stars exhibiting near-degenerate $\ell = 1$ modes (using the full formalism or for instance relying on Eq. (A.8), see also Ahlborn et al. 2025).

Acknowledgements. We thank the referee for their careful and constructive report, which has substantially enhanced both the quality and clarity of the manuscript. L. Bugnet and L. Einramhof gratefully acknowledge support from the European Research Council (ERC) under the Horizon Europe programme (Calcifer; Starting Grant agreement N°101165631). While partially funded by the European Union, views and opinions expressed are, however, those of the authors only and do not necessarily reflect those of the European Union or the European Research Council. Neither the European Union nor the granting authority can be held responsible for them. The authors acknowledge the great support and feedback provided during the redaction of this article by Pr. Rafael García and Pr. Savita Mathur. We would also like to thank Dr. Emily Hatt for her insights on uncertainty estimates. The authors also thank the members of the Asteroseismology and Stellar Dynamics group of the Institute of Science and Technology Austria (ISTA) for very useful discussions: L. Barrault, S.B. Das, K. Smith. This paper includes data collected by the *Kepler* mission and obtained from the MAST data archive at the Space Telescope Science Institute (STScI). Funding for the *Kepler* mission is provided by the NASA Science Mission Directorate. STScI is operated by the Association of Universities for Research in Astronomy, Inc., under NASA contract NAS 5–26555. *Software:* AstroPy (Astropy Collaboration 2013, 2018), Matplotlib (Hunter 2007), NumPy (Harris et al. 2020), SciPy (Virtanen et al. 2020), emcee (Foreman-Mackey et al. 2013), celerite (Foreman-Mackey et al. 2017), slepc4py (Dalcin et al. 2011; Hernandez et al. 2005), KADACS (García et al. 2011), sloscillations (Kuszlewicz et al. 2019, 2023).

References

Aerts, C., Christensen-Dalsgaard, J., & Kurtz, D. W. 2010, Asteroseismology (Springer Science+Business Media B.V.)
Ahlborn, F., Joel Ong, J. M., Van Beeck, J., et al. 2025, A&A, 704, A230
Appourchaux, T. 2020, A&A, 642, A226
Astropy Collaboration (Robitaille, T. P., et al.) 2013, A&A, 558, A33
Astropy Collaboration (Price-Whelan, A. M., et al.) 2018, AJ, 156, 123
Basu, S., & Chaplin, W. J. 2017, Asteroseismic Data Analysis: Foundations and Techniques, Princeton Series in Modern Observational Astronomy (Princeton: Princeton University Press)
Beck, P. G., Bedding, T. R., Mosser, B., et al. 2011, Science, 332, 205
Belkacem, K., Marques, J. P., Goupil, M. J., et al. 2015, A&A, 579, A30
Benomar, O., Bedding, T. R., Mosser, B., et al. 2013, ApJ, 767, 158
Bhattacharya, S., Das, S. B., Bugnet, L., Panda, S., & Hanasoge, S. M. 2024, ApJ, 970, 42
Bordadágua, B., Ahlborn, F., Coppée, Q., et al. 2025, A&A, 699, A310
Borucki, W. J., Koch, D., Basri, G., et al. 2010, Science, 327, 977
Breton, S. N., García, R. A., Ballot, J., Delsanti, V., & Salabert, D. 2022, A&A, 663, A118
Bugnet, L. 2022, A&A, 667, A68
Bugnet, L., Prat, V., Mathis, S., et al. 2021, A&A, 650, A53
Ceillier, T., Eggenberger, P., García, R. A., & Mathis, S. 2013, A&A, 555, A54
Corsaro, E., Stello, D., Huber, D., et al. 2012, ApJ, 757, 190
Dalcin, L. D., Paz, R. R., Kler, P. A., & Cosimo, A. 2011, Adv. Water Resour., 34, 1124
Das, S. B., Einramhof, L., & Bugnet, L. 2024, A&A, 690, A217
Decressin, T., Mathis, S., Palacios, A., et al. 2009, A&A, 495, 271
Deheuvels, S., García, R. A., Chaplin, W. J., et al. 2012, ApJ, 756, 19
Deheuvels, S., Doğan, G., Goupil, M. J., et al. 2014, A&A, 564, A27
Deheuvels, S., Ballot, J., Beck, P. G., et al. 2015, A&A, 580, A96
Deheuvels, S., Ouazzani, R. M., & Basu, S. 2017, A&A, 605, A75
Deheuvels, S., Li, G., Ballot, J., & Lignières, F. 2023, A&A, 670, L16
Di Mauro, M. P., Ventura, R., Cardini, D., et al. 2016, ApJ, 817, 65
Dupret, M., Belkacem, K., Samadi, R., et al. 2009, A&A, 506, 57
Dziembowski, W. A., & Goode, P. R. 1992, ApJ, 394, 670
Eggenberger, P., Montalbán, J., & Miglio, A. 2012, A&A, 544, L4
Eggenberger, P., Lagarde, N., Miglio, A., et al. 2017, A&A, 599, A18
Eggenberger, P., den Hartogh, J. W., Buldgen, G., et al. 2019, A&A, 631, L6
Elsworth, Y., Howe, R., Isaak, G. R., McLeod, C. P., & New, R. 1990, Nature, 345, 322
Fletcher, S. T., Chaplin, W. J., Elsworth, Y., Schou, J., & Buzasi, D. 2006, MNRAS, 371, 935
Foreman-Mackey, D., Hogg, D. W., Lang, D., & Goodman, J. 2013, PASP, 125, 306
Foreman-Mackey, D., Agol, E., Ambikasaran, S., & Angus, R. 2017, AJ, 154, 220
Fuller, J., Lecoanet, D., Cantiello, M., & Brown, B. 2014, ApJ, 796, 17
Fuller, J., Cantiello, M., Stello, D., Garcia, R. A., & Bildsten, L. 2015, Science, 350, 423
Fuller, J., Piro, A. L., & Jermyn, A. S. 2019, MNRAS, 485, 3661
García, R. A., Hekker, S., Stello, D., et al. 2011, MNRAS, 414, L6
García, R. A., Mathur, S., Pires, S., et al. 2014, A&A, 568, A10
García, R. A., Palakkatharappil, D. B., Bugnet, L., et al. 2024, 8th TESS/15th Kepler Asteroseismic Science Consortium Workshop, 123
Gehan, C., Mosser, B., Michel, E., Samadi, R., & Kallinger, T. 2018, A&A, 616, A24
Gizon, L., & Solanki, S. K. 2003, ApJ, 589, 1009
Gomes, P., & Lopes, I. 2020, MNRAS, 496, 620
Gouhier, B., Jouve, L., & Lignières, F. 2022, A&A, 661, A119
Goupil, M. J., Mosser, B., Marques, J. P., et al. 2013, A&A, 549, A75
Goupil, M. J., Catala, C., Samadi, R., et al. 2024, A&A, 683, A78
Grosjean, M., Dupret, M.-A., Belkacem, K., et al. 2014, A&A, 572, A11
Harris, C. R., Millman, K. J., van der Walt, S. J., et al. 2020, Nature, 585, 357
Hatt, E. J., Ong, J. M. J., Nielsen, M. B., et al. 2024, MNRAS, 534, 1060
Hekker, S., & Christensen-Dalsgaard, J. 2017, A&ARv, 25, 1
Hernandez, V., Roman, J. E., & Vidal, V. 2005, ACM Trans. Math. Softw., 31, 351
Hunter, J. D. 2007, Comput. Sci. Eng., 9, 90
Jeffreys, H. 1925, Proc. London Math. Soc., S2–23, 428
Kallinger, T., De Ridder, J., Hekker, S., et al. 2014, A&A, 570, A41
Kuszlewicz, J. S., Chaplin, W. J., North, T. S. H., et al. 2019, MNRAS, 488, 572
Kuszlewicz, J. S., Hon, M., & Huber, D. 2023, ApJ, 954, 152
Li, G., Deheuvels, S., Ballot, J., & Lignières, F. 2022, Nature, 610, 43
Li, G., Deheuvels, S., Li, T., Ballot, J., & Lignières, F. 2023, A&A, 680, A26
Li, G., Deheuvels, S., & Ballot, J. 2024, A&A, 688, A184
Liagre, B., García, R. A., Mathur, S., et al. 2025, A&A, 702, A144
Loi, S. T. 2020a, MNRAS, 493, 5726
Loi, S. T. 2020b, MNRAS, 496, 3829
Lund, M. N., Silva Aguirre, V., Davies, G. R., et al. 2017, ApJ, 835, 172
Lynden-Bell, D., & Ostriker, J. P. 1967, MNRAS, 136, 293
Maeder, A., & Zahn, J.-P. 1998, A&A, 334, 1000
Marques, J. P., Goupil, M. J., Lebreton, Y., et al. 2013, A&A, 549, A74
Mathis, S., & Bugnet, L. 2023, A&A, 676, L9
Mathis, S., & Zahn, J.-P. 2004, A&A, 425, 229
Mathis, S., Bugnet, L., Prat, V., et al. 2021, A&A, 647, A122
Mathur, S., García, R. A., Régulo, C., et al. 2010, A&A, 511, A46
Meduri, D. G., Jouve, L., & Lignières, F. 2024, A&A, 683, A12
Mestel, L., & Weiss, N. O. 1987, MNRAS, 226, 123

Morel, P. 1997, A&AS, 124, 597
Mosser, B., Belkacem, K., Goupil, M. J., et al. 2011, A&A, 525, L9
Mosser, B., Goupil, M. J., Belkacem, K., et al. 2012a, A&A, 548, A10
Mosser, B., Elsworth, Y., Hekker, S., et al. 2012b, A&A, 537, A30
Mosser, B., Vrard, M., Belkacem, K., Deheuvels, S., & Goupil, M. J. 2015, A&A, 584, A50
Mosser, B., Pinçon, C., Belkacem, K., Takata, M., & Vrard, M. 2017a, A&A, 600, A1
Mosser, B., Belkacem, K., Pinçon, C., et al. 2017b, A&A, 598, A62
Mosser, B., Gehan, C., Belkacem, K., et al. 2018, A&A, 618, A109
Moyano, F. D., Eggenberger, P., Salmon, S. J. A. J., Mombarg, J. S. G., & Ekström, S. 2023, A&A, 677, A6
Müller, J., Coppée, Q., & Hekker, S. 2025, A&A, 696, A134
Ong, J. M. J., & Gehan, C. 2023, ApJ, 946, 92
Ong, J. M. J., Bugnet, L., & Basu, S. 2022, ApJ, 940, 18
O'Sullivan, N. K., & Aigrain, S. 2024, MNRAS, 531, 4181
Pereira, F., Campante, T. L., Cunha, M. S., et al. 2019, MNRAS, 489, 5764
Pinçon, C., Belkacem, K., Goupil, M. J., & Marques, J. P. 2017, A&A, 605, A31
Pires, S., Mathur, S., García, R. A., et al. 2015, A&A, 574, A18
Rauer, H., Catala, C., Aerts, C., et al. 2014, Exp. Astron., 38, 249
Ricker, G. R., Winn, J. N., Vanderspek, R., et al. 2014, SPIE Conf. Ser., 9143, 20
Rogers, T. M., & Ratnasingam, R. P. 2025, ApJ, 983, L38
Schatzman, E. 1993, A&A, 279, 431
Schwarz, G. 1978, Ann. Stat., 6, 461
Shibahashi, H. 1979, PASJ, 31, 87
Skoutnev, V. A., & Beloborodov, A. M. 2025a, ApJ, 989, L4
Skoutnev, V. A., & Beloborodov, A. M. 2025b, ApJ, 988, 195
Spruit, H. C. 2002, A&A, 381, 923
Stello, D., Cantiello, M., Fuller, J., et al. 2016a, Nature, 529, 364
Stello, D., Cantiello, M., Fuller, J., Garcia, R. A., & Huber, D. 2016b, PASA, 33, e011
Takahashi, K., & Langer, N. 2021, A&A, 646, A19
Takata, M. 2016a, PASJ, 68, 91
Takata, M. 2016b, PASJ, 68, 109
Tassoul, M. 1980, ApJS, 43, 469
Tayler, R. J. 1973, MNRAS, 161, 365
Toutain, T., & Appourchaux, T. 1994, A&A, 289, 649
Unno, W., Osaki, Y., Ando, H., Saio, H., & Shibahashi, H. 1989, Nonradial Oscillations of Stars (Berlin: Springer-Verlag)
van Lier, T., Müller, J., & Hekker, S. 2025, A&A, 700, A1
Virtanen, P., Gommers, R., Oliphant, T. E., et al. 2020, Nat. Meth., 17, 261
Wentzel, G. 1926, Zeitschrift fur Physik, 38, 518
Woodard, M. F. 1984, Ph.D. Thesis, University of California, San Diego
Zahn, J.-P. 1992, A&A, 265, 115
Zahn, J.-P., Brun, A. S., & Mathis, S. 2007, A&A, 474, 145

Appendix A: Perturbative treatment of the near degeneracy effects

Although not used for our study, we provide in this appendix an explicit approximation to the solution of the eigenvalue problem, as it could be used as a simpler and faster implementation of the near degeneracy effects when they are not strong. In particular, we show how we can use perturbative methods to approximate the eigenvalues of the quadratic eigenvalue problem (Eq. 9). This approach provides closed-form solutions that are valid in the regime of weak near-degeneracy, i.e. when the off-diagonal entries of R are small compared to the diagonal one but not negligible (typically one order of magnitude less). In addition, we demonstrate that it offers a new way to determine both the core and envelope rotation rates from a single near-degeneracy–asymmetric splitting.

The quadratic eigenvalue problem is equivalent to solving the following set of coupled equations:

$$-\omega^2 a_i + \omega \sum_j R_{i,j} a_j + \omega_{0,i}^2 a_i = 0\,, \forall i. \tag{A.1}$$

Since at first order the splittings are symmetrical and the off diagonal terms decrease rapidly, we expect $\sum R_{i,j} a_j \sim R_{i,i} a_i$ and because $|R_{ii}| \ll \omega_{0,i}$, at the zeroth order $\omega = \omega_{0,i}$ (where we chose the positive branch of solutions). Hence, injecting the zeroth-order solution into each equation of the system yields that it can be approximated by

$$-\omega^2 a_i + \omega_{0,i} \sum_j R_{i,j} a_j + \omega_{0,i}^2 a_i = 0\,, \forall i. \tag{A.2}$$

This can be expressed as a matrix equation, for example,

$$A\boldsymbol{a} = \omega^2 \boldsymbol{a}, \tag{A.3}$$

with

$$A_{ij} = \omega_{0,i}^2\, \delta_{i,j} + \omega_{0,i} R_{i,j}. \tag{A.4}$$

Then, using quantum perturbation theory, we find an explicit approximate solution to this eigenvalue problem, yielding the following expression for the frequencies:

$$\begin{aligned} \nu_{i,m}^2 \approx\ & \nu_{i,0}^2 \\ & + 2m\nu_{i,0}\left(\zeta_i\left(1-\frac{1}{L^2}\right)\frac{\Omega_{\rm core}}{2\pi} + (1-\zeta_i)\frac{\Omega_{\rm env}}{2\pi}\right) \\ & + \left(\frac{\Omega_{\rm core}}{2\pi} - \frac{L^2}{L^2-1}\frac{\Omega_{\rm env}}{2\pi}\right)^2 \sum_{i\neq j} \frac{4m^2\nu_{i,0}^2\gamma_{c,ij}^2}{\nu_{i,0}^2 - \nu_{j,0}^2}. \end{aligned} \tag{A.5}$$

This shows that the asymmetry in the splitting due to the near degeneracy is a second-order effect. This formulation allowed us to define an asymmetry parameter for one splitting:

$$\begin{aligned} \delta_{\rm asym} &= \sqrt{\left|\frac{\nu_{i,-m}^2 + \nu_{i,m}^2 - 2\nu_{i,0}^2}{8m^2\nu_{i,0}^2}\right|} \\ &= \sqrt{\sum_{i\neq j}\frac{\gamma_{c,ij}^2}{|\nu_{i,0}^2 - \nu_{j,0}^2|}}\left(\frac{\Omega_{\rm core}}{2\pi} - \frac{L^2}{L^2-1}\frac{\Omega_{\rm env}}{2\pi}\right) \\ &= \alpha\left(\frac{\Omega_{\rm core}}{2\pi} - \frac{L^2}{L^2-1}\frac{\Omega_{\rm env}}{2\pi}\right). \end{aligned} \tag{A.6}$$

We can also recover the symmetric splitting that would occur without near-degeneracy effects:

$$\begin{aligned} \delta\nu_{\rm sym} &= \frac{\nu_{i,m}^2 - \nu_{i,-m}^2}{4|m|\nu_{i,0}} \\ &= \left(1-\frac{1}{L^2}\right)\zeta_i\frac{\Omega_{\rm core}}{2\pi} + (1-\zeta_i)\frac{\Omega_{\rm env}}{2\pi}. \end{aligned} \tag{A.7}$$

If we further define $\beta = \frac{L^2}{L^2-1}\alpha$, $\eta = \frac{L^2-1}{L^2}\zeta_i$, $\lambda = (1-\zeta_i)$, the two parameters $\delta_{\rm asym}$ and $\delta\nu_{\rm sym}$ can be linearly combined to obtain the core and envelope rotational rates from only one splitting. The appropriate linear combinations are the following:

$$\begin{cases} \dfrac{\Omega_{\rm core}}{2\pi} = \dfrac{1}{\alpha\lambda+\beta\eta}\left(\lambda\delta_{\rm asym} + \beta\delta\nu_{\rm sym}\right) \\ \dfrac{\Omega_{\rm env}}{2\pi} = \dfrac{1}{\alpha\lambda+\beta\eta}\left(-\eta\delta_{\rm asym} + \alpha\delta\nu_{\rm sym}\right). \end{cases} \tag{A.8}$$

This shows that in the case of a splitting with near-degeneracy effects, both the envelope and core rotation rates are encoded simultaneously in the morphology of the splitting. Without near-degeneracy effects as usually studied in $\ell = 1$ modes, we can only access a linear combination of both rotation rates, and two multiplets (ideally one p and one g dominated) are needed to constraint both the core and the envelope rotations.

Appendix B: Vetting the asymptotic formulation

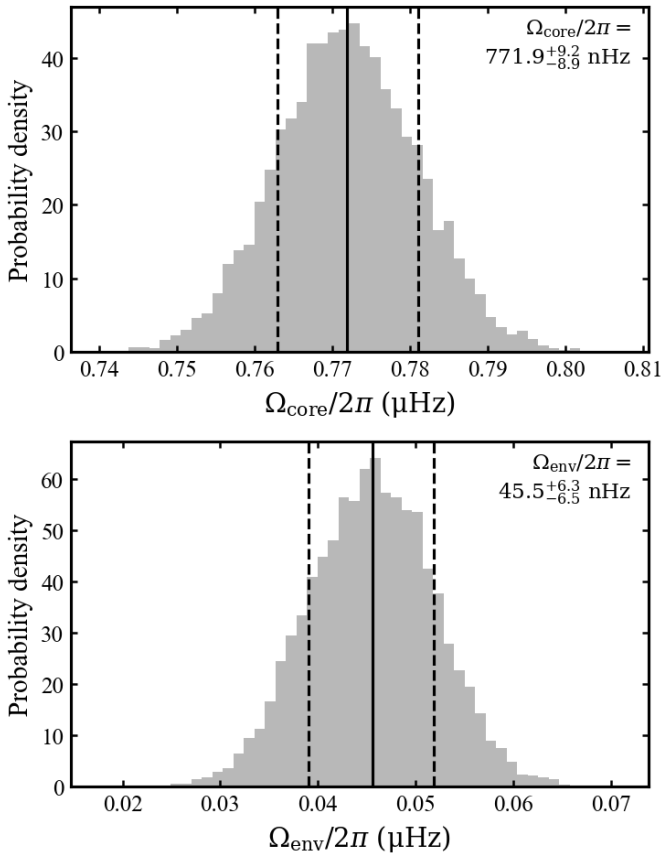

Fig. B.1. Histograms showing the result of the Monte-Carlo analysis with the asymptotic formulation.

To propagate the observational uncertainties of the mixed-mode parameters into the inferred rotational components, we performed a Monte-Carlo analysis with $N = 10,000$ realisations. For each realisation, we randomly drew the parameters $(\nu_a, \nu_b, \Delta\Pi_2, \zeta_a, \zeta_b)$ from independent Gaussian distributions centred on the value reported in Deheuvels et al. (2017) and with their respective uncertainties. For every random draw, we then minimised the χ^2 difference between the observed multiplet frequencies and the model frequencies computed following Sect. 2.3.2, treating $\Omega_{\rm core}$ and $\Omega_{\rm env}$ as free parameters. The optimisation was carried out using the L-BFGS-B algorithm, with the bounds $\nu_c \in [0, 1]\,\mu$Hz and $\nu_{\rm env} \in [0, 0.1]\,\mu$Hz. Only successful minimisations were retained in the final sample. The resulting posterior distributions of ν_c and $\nu_{\rm env}$ were summarised by their median values and their 16th–84th percentile ranges, which we report as our final uncertainties.

Appendix C: Bayesian priors

C.1. Priors on pressure mode and mixed $\ell = 1$ modes parameters

The frequency of maximum power $\nu_{\rm max}$ is fixed to the value given by PyA2Z, while we assign flat priors within ±5% of the initial guess for $\Delta\nu$ and $\Delta\Pi_1$ to account for the uncertainties of the PyA2Z pipeline, and we chose not to constrain ε, as its value is highly sensitive to any change in $\Delta\nu$. We assigned the priors on $\delta\nu_{0,\ell}$ around the values predicted by scaling relations provided by Mosser et al. (2018), Corsaro et al. (2012). We assigned to q_1 a flat prior between 0.15 and 0.4 based on the results of previous studies such as Mosser et al. (2017a), Kuszlewicz et al. (2023).

For $\varepsilon_{\rm g,1}$, we chose a very uninformative flat prior between 0 and 1. In the same fashion we chose very uninformative flat priors for $\beta_{0,\ell}$ and α between −0.1 and 0.1. This range seemed appropriate as the α and $\beta_{0,\ell}$ parameters found by Appourchaux (2020) and Lund et al. (2017) in the same evolutionary stage were under 10^{-2}. We assigned flat priors for rotation rates, with values ranging from 0 to 1,000 nHz for the core and 0 to 100 nHz for the envelope. These core rotation prior was derived from the work of Deheuvels et al. (2017) for KIC 7341231 and informed by a visual inspection of the splittings observed in KIC 8179973. For the envelope rotation, we again utilised the Deheuvels et al. (2017) article for KIC 7341231, and assumed a core envelope contrast of at least 10 in KIC 8179973. All of those priors are summarised in table C.1.

C.2. Priors on KIC 7341231

A global analysis using PyA2Z gives $\Delta\nu$, $\nu_{\rm max}$, and a guess value of $\Delta\Pi_1$ using the stretched period method. The priors on those parameters were then chosen according to Sect. C.1. Refined values of $\Delta\Pi_1$ and $\Delta\nu$ are obtained by fitting the mixed $\ell = 1$ modes according to the method described in Sect. 3.2.7.Because the angle of inclination is high, we had access to the $m = 0$ components of each quintuplet. Hence, we decided to use the method described in 3.2.4 to constrain q_2. To use this method, we needed to access the following parameters and their associated uncertainties: $\Delta\Pi_2$, $\Delta\nu$, ν_a, ν_b and the position of the $\ell = 2$ p mode that is given by $\nu_0 - \delta\nu_{0,2}$. Where ν_a and ν_b are the positions of the $m = 0$ components of each multiplet and ν_0 is the frequency of the closest radial mode. $\Delta\Pi_2$ and its associated uncertainty was then obtained following Sect. 3.2.2. In order to obtain $\delta\nu_{0,2}$, we fitted a bimodal Gaussian model to the averaged collapse of the echelle diagram. We obtained $\delta\nu_{0,2}/\Delta\nu = 0.120 \pm 0.002$. We finally peakbagged ν_a, ν_b and ν_0 and obtained $\nu_a = 380.382 \pm 0.023\,\mu$Hz, $\nu_b = 382.627 \pm 0.01\,\mu$Hz, and $\nu_0 = 384.514 \pm 0.011\,\mu$Hz. Using those values and their uncertainties, we can use a Monte-Carlo method to sample the distribution of q_2 according to equation (42). We obtained $q_2 = 0.041 \pm 0.003$. We decided to use a uniform prior on q_2 within 3 sigma of the obtained value.

Furthermore, since we are only interested in reproducing the frequencies of the star's modes and an angle of inclination was already fitted by Deheuvels et al. (2012), we adopt a fixed angle of inclination of 85°, in order to limit the number of free parameters.

Table C.1. Flat prior ranges for the global fit of KIC 7341231 and KIC 8179973.

Prior \ Star	KIC 7341231	KIC 8179973
$\nu_{\rm max}$ (μHz)	408 (fixed)	347 (fixed)
$\Delta\nu$ (μHz)	29.1 ± 5%	23 ± 5%
ε	0 < 1	0 < 1
$\delta\nu_{0,1}$ (μHz)	-1 < 1	-1 < 1
$\delta\nu_{0,2}$ (μHz)	2 < 3	2 < 3
$\beta_{0,2}$	-0.1 < 0.1	-0.1 < 0.1
$\Delta\Pi_1$ (s)	104.5 < 115.5	92 < 102
q_1	0.15 < 0.4	0.15 < 0.4
$\varepsilon_{\rm g,1}$	0 < 1	0 < 1
$\Delta\Pi_2$ (s)	$\Delta\Pi_1/\sqrt{3} \pm 5\%$	$\Delta\Pi_1/\sqrt{3} \pm 5\%$
q_2	0.041 ± 0.009	< 0.107
$\varepsilon_{\rm g,2}$	0 < 1	0 < 1
$\Omega_{\rm core}/2\pi$ (nHz)	<1,000	<1,000
$\Omega_{\rm env}/2\pi$ (nHz)	<100	<100
α	-0.1 < 0.1	-0.1 < 0.1
$\beta_{0,1}$	-0.1 < 0.1	-0.1 < 0.1

C.3. Priors on KIC 8179973

A global analysis using PyA2Z gives $\Delta\nu$, $\nu_{\rm max}$, and a guess value of $\Delta\Pi_1$ using the stretched period method. The priors on those parameters were then chosen according to Sect. C.1. Refined values of $\Delta\Pi_1$, $\Delta\nu$ and a value of q_1 are obtained by fitting the mixed $\ell = 1$ modes according to the method described in Sect. 3.2.7. In KIC 8179973, the angle of inclination is such that the m=0 modes of the $\ell = 2$ quintuplet are either absent or buried in the noise of the star. Hence, we cannot use the same method as the on used for KIC 7341231 to constrain q_2. However, we can still use simple analytical arguments to put a rough upper bound on q_2 as a function of q_1.

q_1 in itself is obtained by fitting the mixed $\ell = 1$ modes according to the method described in Sect. 3.2.7. We obtain $q_1 = 0.197 \pm 0.001$ which yields that $q_2 < 0.107$ using the arguments presented in Sect. 3.2.5. We use a uniform prior for the orientation of axis of rotation of the star with respect to the line of sight. This translates to a prior $\propto \sin(\theta_{\rm inc})$ for $\theta_{\rm inc}$ between 0° and 90°.

C.4. Corner plots and comparison data-model

We compared the frequencies obtained within our asymptotic Bayesian framework to the frequencies obtained by Deheuvels et al. 2012, 2017 using a peakbagging code. Both the asymptotic model and the peakbagged frequencies agree, particularly around the central frequency ($\nu_{\rm max}$) as can be seen

on figure C.1. This congruence is expected, as the asymptotic approximation becomes less precise further from $\nu_{\max}$ due to increasing sensitivity to surface effects. Crucially, the physically informed nature of our method allows it to account for small excesses of power that are often indistinguishable from noise in standard peakbagging procedures.

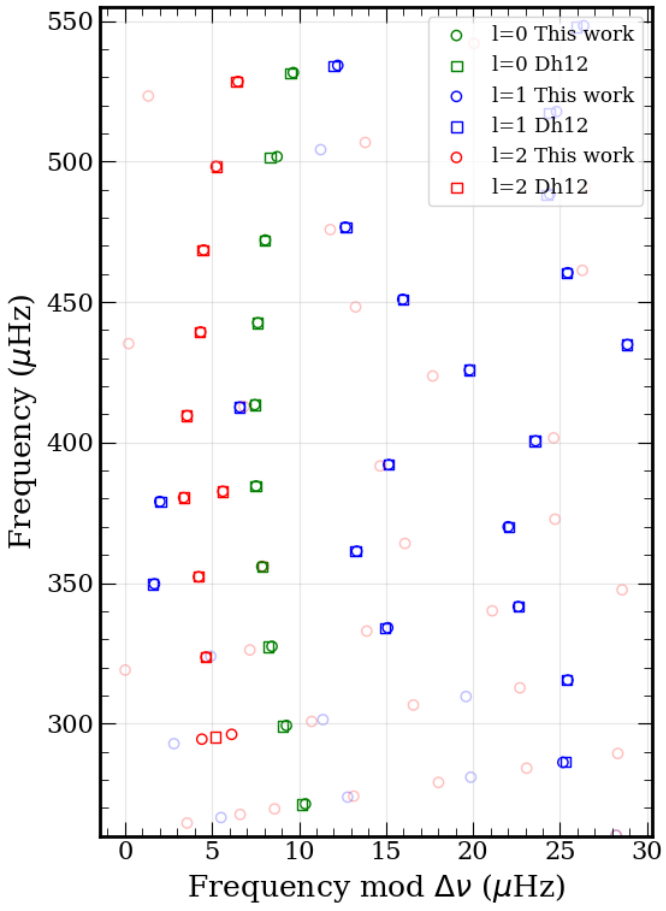

Fig. C.1. Echelle diagram comparing the oscillation frequencies derived from the Bayesian asymptotic model (circles, this work) with the peakbagged frequencies of KIC 7341231 (squares, Deheuvels et al. 2012, 2017, referred to as Dh12 in the legend of the figure). The markers for the model frequencies are rendered semi-transparent when the separation from a peakbagged frequency exceeds 1 μHz.

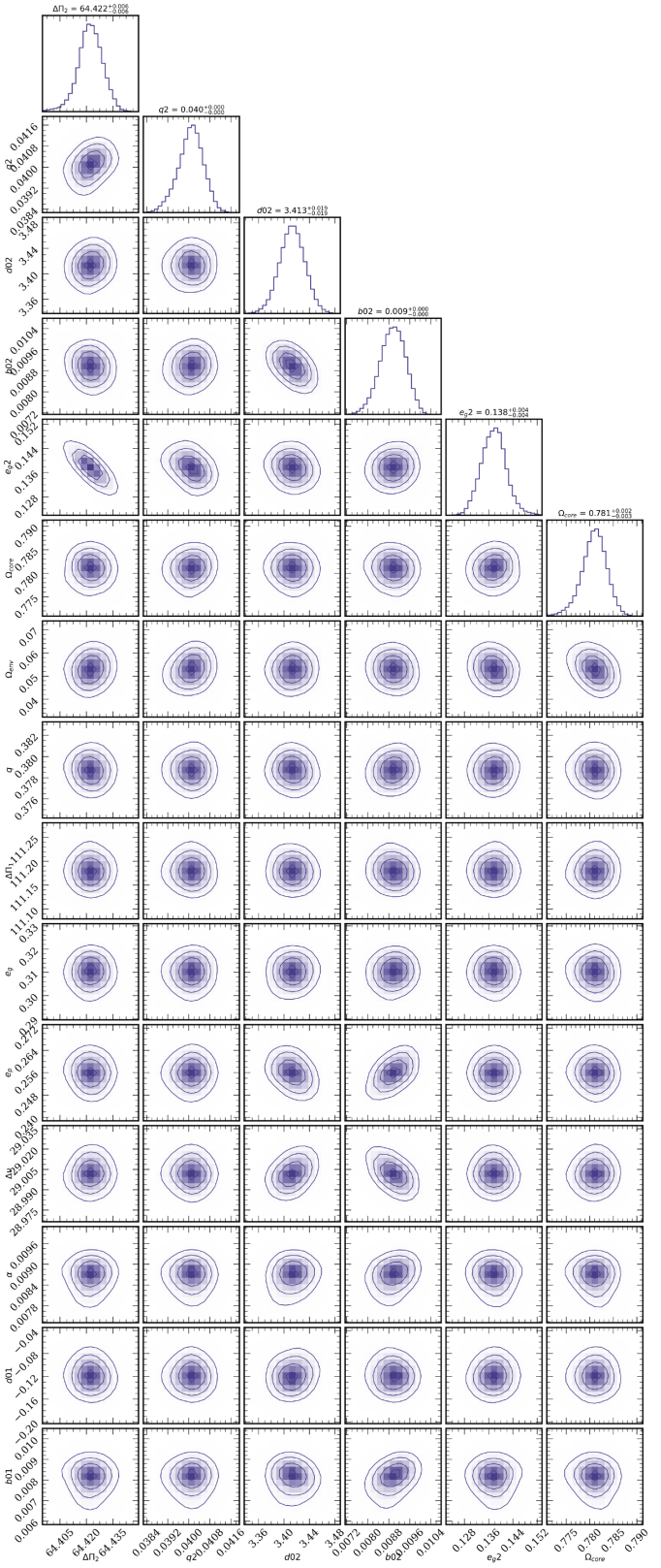

Fig. C.2. Corner plot of the Bayesian fit of all the parameters for KIC 7341231 (first part).

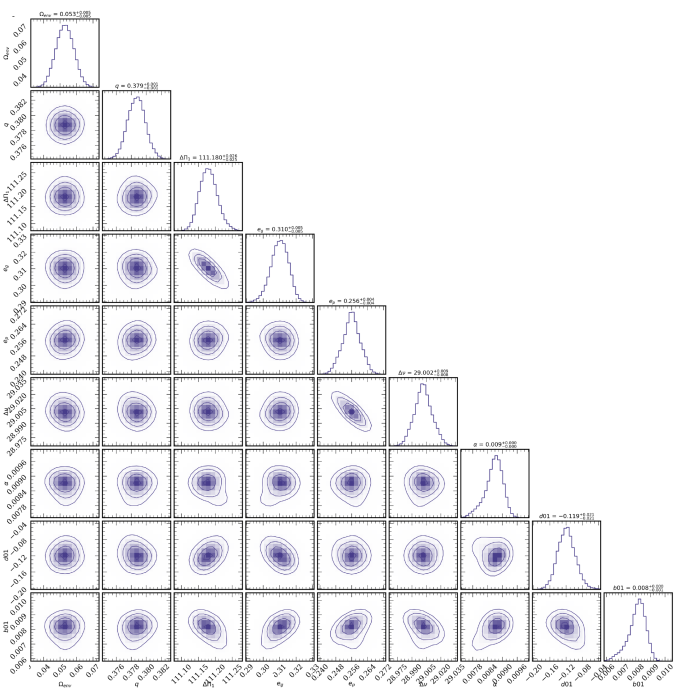

Fig. C.3. Corner plot of the Bayesian fit of all the parameters for KIC 7341231 (second part).

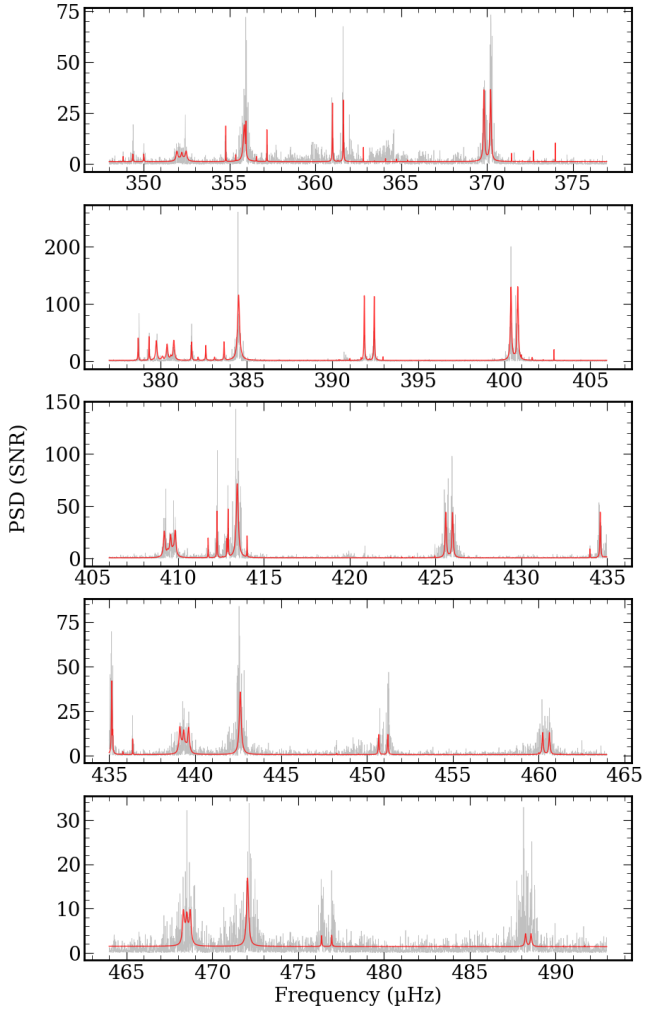

Fig. C.4. Echelle diagram showing the superimposed data and asymptotic model for the most prominent modes of KIC 7341231.

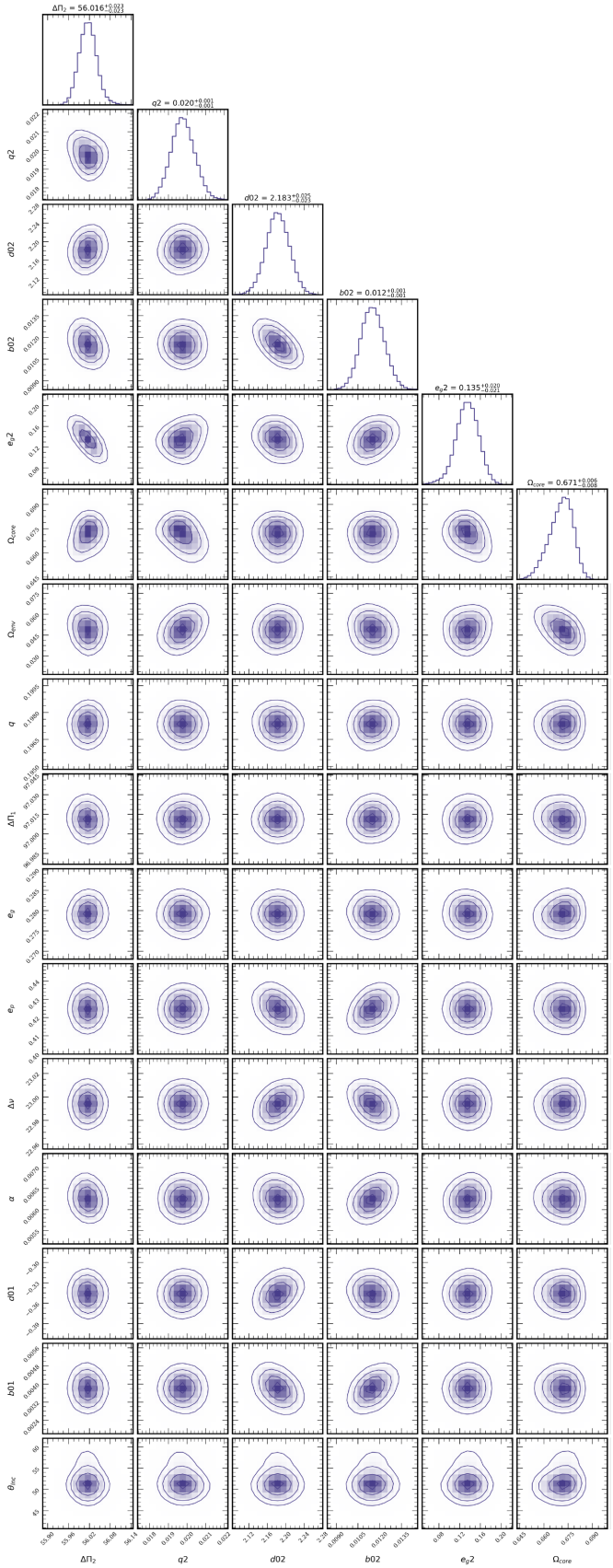

Fig. C.5. Corner plot of the Bayesian fit of all the parameters for KIC 8179973 (first part).

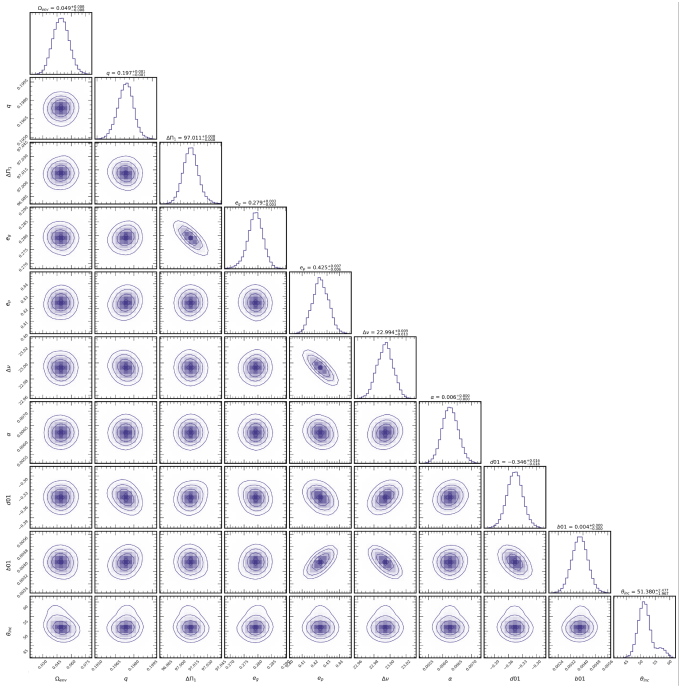

Fig. C.6. Corner plot of the Bayesian fit of all the parameters for KIC 8179973 (second part).

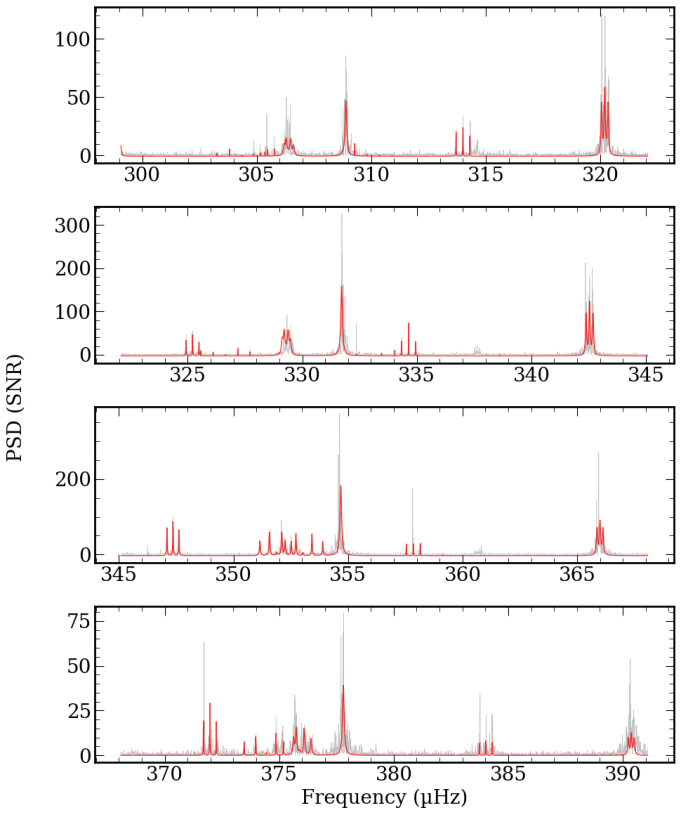

Fig. C.7. Echelle diagram showing the superimposed data and asymptotic model for the most prominent modes of KIC 8179973.